REPORT DOCUMENTATION PAGE

Form Approved
OMB No. 0704-0188

1. AGENCY USE ONLY *(Leave blank)*

2. REPORT DATE
July 1995

3. REPORT TYPE AND DATES COVERED
Final Report, Nov. '91 - Dec. '94

4. TITLE AND SUBTITLE
Synthesis of Nanocrystalline Nb-Aluminides by Laser Ablation Technique

5. FUNDING NUMBERS
61102F 503700

6. AUTHOR(S)
Professor J. Mazumder, Dr. T. Duffey, T. Yamamoto and H. Chung

7. PERFORMING ORGANIZATION NAME(S) AND ADDRESS(ES)
Professor Jyoti Mazumder
Univ of Illinois - Urbana Champaign
801 South Wright Street
Champaign, IL 61820-6242

AFOSR-TR-~~96~~ 97
0027

9. SPONSORING/MONITORING AGENCY NAME(S) AND ADDRESS(ES)
Captain Charles Ward
AFOSR/NE
Building 410, Bolling AFB DC
20332-6448 .

10. SPONSORING/MONITORING AGENCY REPORT NUMBER
F49620-92-J-0142

11. SUPPLEMENTARY NOTES

12a. DISTRIBUTION/AVAILABILITY STATEMENT
APPROVED FOR PUBLIC RELEASE; DISTRIBUTION IS UNLIMITED.

12b. DISTRIBUTION CODE

13. ABSTRACT *(Maximum 200 words)*

This report describes research efforts in the synthesis by laser ablation deposition of $NbAl_3$ in nano-crystalline forms, as well as process characterization and modeling. Nanocrystalline powders and films were produced under a range of process conditions. Multilayer structures, alternating Al and $NbAl_3$ films were also fabricated. Process yields ranged over 0.1–0.3 μg/laser pulse. Variations in yield reflect different gas-dynamics at different process conditions. Mean powder particle sizes ranged over 5–10 nm, increasing with gas pressure and decreasing with laser power. The width of size distribution exhibited a similar dependence. Stoichiometric ratio of Al:Nb varied from 2:1 to 3:1, approaching congruence at low laser power and high gas pressure. Absorption spectroscopy of the ablation plume measured Nb atomic densities corresponding to an ablation rate of a few ng/pulse, implying near-complete nucleation within 100 ns. Nonetheless, this signal constitutes a useful monitor of the ablation rate. Temperatures and expansion velocities were also measured via the optical diagnostic; axial expansion velocity correlates well to mean particle size. The numerical model predicted low ion concentration (confirmed by the optical diagnostic) and saturation in the ablation rate at high laser pulse energies due to plasma coupling(confirmed by target mass loss and optical diagnostic).

19970117 064

14. SUBJECT TERMS

15. NUMBER OF PAGES
70

16. PRICE CODE

17. SECURITY CLASSIFICATION OF REPORT
UNCLASSIFIED

18. SECURITY CLASSIFICATION OF THIS PAGE
UNCLASSIFIED

19. SECURITY CLASSIFICATION OF ABSTRACT
UNCLASSIFIED

20. LIMITATION OF ABSTRACT

DTIC QUALITY INSPECTED 1

Synthesis of Nanocrystalline Nb-Aluminides by Laser Ablation Technique

Professor Jyotirmoy Mazumder,
Dr. T. Duffey,
T. Yamamoto and H. Chung
1206 W. Green Street
Urbana, IL 61801

Final Report
submitted to

Air Force Office of Scientific Research
Building 410
Attn: Captain Charles Ward
Bolling Air Force Base
Washington, DC 20332

for research conducted during the period
November, 1991 - December, 1994
Under Contract No. 92-J-0142

University of Illinois
1995

Center For Laser Aided Materials Processing

University of Illinois at Urbana-Champaign

Table of Contents

List of Figures

List of Tables

Executive Summary

Nanocrystalline materials possess a grain or layered structure in the size range of below 50 nm, leading to a large fraction of grain or interphase boundaries. These phases may be of the crystalline, quasicrystalline or of the amorphous form with variable compositions. These atomistically unique structures are expected to exhibit enhanced features in materials properties of the consolidated materials. They are found to have many unique properties such as improved strength, enhanced ductility at room temperature enhanced self-diffusivity reduced density, increase of thermal expansion coefficient, increase of specific heat, and increase of superconducting transition temperature. A number of processing methods have been employed to produce nanocrystalline materials but all suffer from various deficiencies such as purity of materials produced, limitations to specific materials systems (pure elements) and/or low production rates.

Laser ablation is a promising technique for improving the conventional gas condensation method of producing nano-crystalline materials. This method uses a high-intensity laser pulse to remove sputter material from a target in a vapor/plasma plume. The plume material recondenses and deposits on a cooled substrate. The advantages of the ablation technique rest in its abilities to (i) create a much larger flux of evaporated material, (ii) produce plumes of evaporated materials with stoichiometry congruent to the target even for complex chemical systems such as ceramic superconductors, and (iii) be easily and quickly controlled by altering the laser pulse energy, repetition rate, and focus spot size. Thus the potential increases for creating a high-yield, versatile process that introduces no contaminants and synthesizes materials with complex chemical structures.

The goal of the program is to develop a science base for producing nanocrystalline forms of the Nb-aluminide intermetallics. These intermetallics are potentially good prospects for aerospace applications, possessing excellent strength-to-weight ratios and high temperature oxidation resistance. However, their low temperature ductility is limited. Nano-crystalline forms of these materials are expected to improve this property through the availability of grain boundaries for slip-planes. The specific objectives of this research are: (1) a fundamental understanding of the rate of generation of nanocrystalline niobium aluminides by laser ablation with a view to improve upon the rates available from the standard gas condensation technique, (2) on-line measurement of the physical state of the vapor plume during ablation, (3) a correlation between the process parameters and nanocrystal size distribution, yield and properties, (4) the

stability, microstructure and grain growth of these materials, (5) correlation of on-line diagnostics to properties of nanocrystalline powders produced.

This report summarizes experimental and theoretical studies carried out during the period of November 1991 to December 1994 on production of nano-crystalline $NbAl_3$ for improved low temperature ductility with minimal sacrifice of environmental resistance at high temperature. A process chamber for producing nano-crystalline $NbAl_3$ was designed and constructed. Nano-crystalline powders and thin films were fabricated over a range of processing conditions. The process was characterized in terms of ablation rate, yield and collection efficiency. Materials produced were characterized in terms of particle size distribution, composition and crystal structure. Process and materials results were correlated to changes in process variables Simultaneous to the process runs, an optical diagnostic, based on laser absorption was used to measure density, temperature and velocities of the vapor plume. Trends between these data and the properties of the material produced were established. A theoretical model was established to simulate the process.

The objective of the process and characterization work was to demonstrate the feasibility of laser ablation as a nano-crystalline material production technique and reach an understanding of the effects on materials properties and process yield caused by varying the process parameters. Ablation experiments were carried out under nine distinct process conditions. Target and substrates masses weighed prior to and after each process run; the mass differentials were used to calculate ablation and deposition (yield) rates per laser pulse. TEM images were used to establish particle size distributions of the materials. Select area X-ray diffraction from the same area as the TEM image was taken to determine the crystal structure. Large area X-ray diffraction was employed as more comprehensive measurement of particle sizes. Microchemical analyses of the powders, to establish composition from characteristic X-ray intensities for each element, were performed using a TEM equipped with energy dispersive spectroscopy (EDS).

Various trends among these data were identified. Ambient process chamber pressures of at least 1.0 Torr are necessary for powder synthesis; below this value fine-grained thin films result. Ablation rate changes little with gas pressure, more strongly with laser pulse energy. Process yield (collection efficiency) is strongly dependent on gas pressure. Particle size distributions are revealed by X-ray diffraction to have a bimodal distribution composed of particle with mean diameters of a few nanometers and particles with diameters in the 75–200 nm range, dependent of process parameters. In general, both these distributions produce smaller particles at lower gas pressures and higher laser energies. Particle size is more sensitively dependent on gas pressure than laser energy within the range of process variables tried. Volume ratios of these two distributions within the material produced are approximately 1:1. TEM micrographs provide detailed characterization of the size distribution of the smaller-mode of particles. The distribution width of this mode is quite small (variance as low as 2.4), but increases with pressure. At the highest pressure studied, the distribution width decreased sharply with increasing laser energy. Crystal structures from select area X-ray diffraction patterns were observed to be that of $NbAl_3$ (DO_{22}) for all process conditions. Lattice parameter values matched well with reported values for bulk $NbAl_3$. Composition measurements revealed a variation in Al:Nb atomic ratios ranging from 2:1 to exactly stoichiometric 3:1; stoichiometric congruence was more nearly achieved at higher gas pressures and lower laser energies. The dependence on laser energy saturated for the higher laser energies.

The laser ablation apparatus was also modified to produce multilayer thin films of $NbAl_3$ and Al. It was demonstrated that films with excellent homogeneity and individual layer thicknesses of less than 10 nm could be quickly deposited on a silicon substrate.

The main scientific achievements of the process and characterization work are: production of nano-crystalline powders and thin films of $NbAl_3$ and development of understanding of process relationships governing production of such materials.

The objective of the optical diagnostic technique was to gain insight into the physical processes determining the production of nano-crystalline materials, and to identify signal characteristics useful for process monitoring and control. A tunable dye laser was directed through the ablation plume to probe spectral transitions in neutral Nb atoms within the plume. Methods were developed for measuring Nb atomic density, excitation temperature, and axial and transverse velocities. Peak densities in the range of 10^{10}–10^{11} cm^{-3} were observed; these imply total Nb masses within the plume in the range of 5–20 nanograms. This suggests that ablated material either leaves the target in predominantly molecular form or condenses from atomic vapor into molecules and clusters within 100 ns of the end of the ablation laser pulse. These rates nonetheless correlate well with the ablation rates as measured by target mass differential. Excitation temperatures are measured in the 2000–7000 K range. Expansion velocity of the plume along the axial direction is measured to vary over $2–8 \times 10^5$ cm/sec. In general, this velocity increases with laser energy and decreases with gas pressure, leading to the conclusion that increasing laser pulse energy leads to increased kinetic energy of the ablated material. Radial expansion front velocities exhibit similar results. The axial front expansion velocity is shown to vary inversely to the mean particle size of powder produced for process conditions of constant He pressure and variation in ablation laser pulse energy. The distribution of radial velocities of individual atoms is also measured.

These values exceed the expansion front velocities by factors of 2–3, suggesting that expansion is essentially diffusive rather than free. In addition, the distribution shape suggests that a kinetic-energy temperature may be assigned. These temperatures exceed the excitation temperatures by factors as large as 100. It is theorized that the discrepancy reflects inefficient energy transfer between electron and atom kinetic energy distributions.

The main scientific findings of the diagnostic work are: density measurements suggest that nucleation occurs on time scales of less than 100 ns, absorption signal may be used to monitor ablation rates and particle sizes, well-defined excitation and kinetic temperatures exist within the plume, but are vastly unequal.

The objective of the modeling work was to provide a method to predict process results from minimal experimentation. A gas-dynamical model was developed for analyzing plasma formation and velocity and particle-size distributions in the plasma during laser ablation. The melting and evaporation rates are determined by using the heat conduction equation and the Stefan condition. Gas-dynamics equations are solved to study the convective flow of the metal particles in the region above the Knudsen layer. Plasma physics is used to model plasma formation and to compute the laser-beam attenuation coefficient and ion concentration within the plasma. The particle-size distribution in the plasma is determined by using a droplet-growth theory. The model predicted that significant droplet growth would occur even in vacuum within the duration of the ablation laser pulse. It predicted a saturation in the ablation rate with increasing laser pulse energy, in accord with observations. Predicted excitation temperatures within the plasma were of the same order of magnitude as measured by the optical diagnostic. The most significant scientific achievement of this work is the development of a model for nano-crystalline ablation synthesis which will improve understanding of the evaporation and nucleation aspects of the process.

There has been considerable interplay between results from the three lines of research. The absorption spectroscopy signal provides a means to monitor ablation rate in real time. This signal, in combination with understanding derived from the process characterization data (e.g. the relation between collection efficiency and gas pressure) would permit the design of a closed-loop system to maintain constant deposition rate despite changes in the process environment (such as decay in optical transmission of the window through which the ablation laser beam enters the process chamber, or rise in chamber pressure due to heating). A detailed consideration of the results of spectroscopy and microcharacterization leads to a proposed method for monitoring particle size by time-of-flight measurements. Comparison of the model and process data explain variations in the ablation rate with power as being due to increased plasma coupling of the ablation beam. The spectroscopy data help to validate the model by confirming model predictions that nucleation into nano-size grains occurs within a few tens of nanoseconds. Also, the model's prediction of low ion concentration is supported by the inability of the spectroscopy apparatus to obtain absorption at a wavelength corresponding to an ion spectral line.

This project has led to significant advancement of the science base for laser synthesis of nano-crystalline materials. This is reflected in the various publications derived from this work. A list of publications proceeding from this project is provided in Appendix A.

Chapter 1. Introduction

Nanocrystalline materials have grain or layered structure in the size range of less than 50 nm and have a large fraction of grain or interphase boundaries. These phases may be of the crystalline, quasicrystalline or of the amorphous form with variable compositions[1, 2]. These atomistically unique structures and chemical compositions as well as their nano-scale natures are expected to exhibit enhanced features in materials properties of the consolidated materials.

So far, considerable amounts of effort have been devoted to characterization of the nanocrystalline materials and their consolidated bulk materials as well as their synthesis methods. They are found to have many unique properties such as improved strength, enhanced ductility at room temperature [3], enhanced self - diffusivity reduced density, increase of thermal expansion coefficient[4], increase of specific heat[4], and increase of superconducting transition temperature[5]. These promising properties of nanocrystalline materials have accelerated the development of the synthesis methods of nanocrystals. Various processing methods presented to date include gas condensation[6], mechanical alloying[7], chemical vapor deposition[8], magnetron sputtering[9], and plasma reaction[10]. Considering the present problems and further applications, a processing method must be developed bearing the following conditions: 1) High production rate, 2) Near exact conversion of the composition of the bulk source materials into nanocrystalline powders, 3) Clean and uncontaminated powders by maintenance of a pristine process environment, 4) Ease of control of various processing variables, 5) Potential possibilities to produce powders from any composition and with any microscopic state such as nonequilibrium multi-component alloys and ceramics, 6) Narrow particle size distributions, 7) Crystal structure manipulation. However, none of the present methods for producing nanocrystalline materials suitably satisfy all the above conditions.

From this perspective, laser ablation vaporization in conjunction with gas-condensation may be the most promising candidate to respond to all of the above requirements. In conventional gas condensation, the evaporated or sputtered atoms from the bulk material collide with the ambient gas atoms, which may be inert gases (He, Ne, Ar, Kr, Xe, Rn, etc.) or reactive gases (H, B, N, O, F, etc.) depending on the final products and compositions desired. Through collisions, the ejected atoms lose their energy rapidly and eventually condense to form a cloud made up of small nano-scale powders. In this method, any kind of irradiation source able to eject atoms from the bulk material into the gas-filled space can be used. However, it should be noted that the choice of the ejecting source strongly effects the production rate and other characteristics of the produced nanocrystalline materials. The ejecting source plays the key role in the process and material evolution.

Conventional resistive heating as with a tungsten filament heater is the most widely used due to its simple experimental set-up[1, 6], although its use is limited to the synthesis of pure metals with relatively low melting points. Recently, many other kinds of ejecting sources have become available through the new technological development. Some of the interesting ejecting sources include DC or RF sputtering[9], electron beam[11], plasma jet flame[10] and laser beam[12]. A laser beam has many different properties compared to other sources: high energy density, pulsed beam with an easily modifiable profile, both temporally and spatially, (even continuous beam), wide range of available wavelengths, high transmission in the atmosphere, monochromatic and coherent beam, and easy handling with relatively inexpensive optics. Stafast and Von Przychowski reported an average laser ablation rate of 1 $mgJ^{-1}cm^{-2}$ for Al_2O_3 using an excimer laser with 248 nm wavelength[13]. Little work on the nanocrystalline material fabrication by the laser ablation has been found in the literature. Laser ablation has been long utilized in the study of clusters which comprise tens of atoms[14]. Recently, Chow *et al.* used laser ablation to evaporate a ceramic target and a Ni alloy disc simultaneously[12]. The result was a mixture of several kinds of fiber-like nanocomposites codeposited on the target. Their report of this work, however, did not pursue a detailed analysis of the material characteristics in correlation with the process variables.

$NbAl_3$, which possesses $D0_{22}$ crystal structure[15], is a candidate for high temperature structural applications because of its high strength-to-weight ratio and oxidation resistance at elevated temperature[16-20]. However, $NbAl_3$ shows limited ductility at room temperature, and has not yet been commercialized. Much efforts have been made to improve this limited ductility using relatively conventional techniques such as alloying of a third element, rapid solidification and laser cladding[19].. As a means to achieve improvement of ductility at room temperature while maintaining oxidation resistance at elevated temperature and the possibility of synthesizing multi-component materials with nonequilibrium chemistry, the synthesis of nanocrystalline $NbAl_3$ using the laser ablation technique presents an intriguing potential for process development.

To date, only mechanical alloying has been used to synthesize $NbAl_3$ nanocrystalline materials[21]. Nanoscale materials synthesized by mechanical alloying were comprised of a mixture of two phases, $NbAl_3$ and Nb_2Al, and are expected to have high strain and contaminations introduced by the strong contact of the powders with the container and balls during processing. We have successfully synthesized nanocrystalline alloy $NbAl_3$ with exact stoichiometry using the newly developed processing method, and have noted that the laser pulse energy and the back-filled gas pressure have a significant influence on the production rate of the powder materials[22].

Most efforts relating to the study of nanocrystalline materials have focused on the characterization of consolidated nanocrystalline materials of pure metals, and little effort has been made to identify the relationships between processing and nanomaterial characteristics which are fundamental to exploit these novel materials. Understanding of the processing methods in relation to the synthesized material properties enables us to produce nanocrystalline materials having the desired properties while simultaneously maximizing yield, hence reducing the processing time.

This report summarizes a three-year research project to explore the synthesis of nano-crystalline $NbAl_3$ materials. A three-pronged approach was taken. First, a process chamber was constructed and process runs were performed to fill out a matrix of process variables. Materials produced in these runs were characterized as to particle size, width of the size distribution, microstructure. These data were then compared to the selected process variables to establish the process relations for optimizing and controlling the process. Simultaneous to process runs, an optical diagnostic technique, laser absorption spectroscopy, was used to probe the physical state of the plume. The intent of these efforts was to gain deeper insight into the fundamental physical processes that determined the final state of material produced, while also developing capabilities for sensors that would permit real-time control and modification of the process. Numerical simulation of the laser-target interaction and particle nucleation process constituted the third line of attack to the problem. The aim here was to shorten process development time by pointing the way to improvements in the process without the need for repetitive and lengthy experimentation. A subsidiary goal was to lay the groundwork for decision-making software algorithms, employing sensor data as inputs, which would vary process parameters to tailor and control the process.

The format of this report is as follows. The following chapter describes in detail the process itself as employed in this work and materials characterization of the nanocrystalline powders. As a coda, there is a section discussing the use of the ablation technique for fabricating fine-grained superlattice thin films, consisting of alternate layers of ductile and brittle materials. Future research will explore further this idea for synthesis of novel nano-crystalline composites. This appears to be a second avenue toward maintaining the desirable properties of intermetallics such as $NbAl_3$ while mitigating their unsatisfactory properties. The ability of our apparatus to produce such multilayers is demonstrated in this section. Chapter 3 summarizes the optical diagnostic work. Chapter 4 describes, in brief, the computer model and its results. A complete discussion of this work is contained in a previous report.[23] Chapter 5 gives a succinct description of preliminary work on laser cladding of NbAl compounds. This research provided an important science base for both the microstructure characterization of the powders and the spectroscopic diagnostics. A full presentation of this portion of the work forms an appendix, in the form of a doctoral dissertation, at the end of this report.

Chapter 2. Synthesis and Characterization of Nanocrystalline $NbAl_3$ by Laser Ablation Technique

In the first part of this chapter, the basics of the laser ablation processing method will be presented along with the design of the ablation system which enables long continuous processing runs. The capability of this system in production of $NbAl_3$ nanocrystalline materials is discussed. Production rate and ablation rate are measured for different process parameter values. These process data help to illuminate how material production is affected by changes in the independent processing parameters. This is important to explore the capabilities of the new process. Production rates (e.g. process yield) were determined by the weighing the collected nanocrystallines, and ablation rates were measured by recording the weight loss of the $NbAl_3$ target before and after each process run.

The objective of the second part of this chapter is to understand the property-structure-processing relationships as fundamental to controlling the entire process. For this purpose, transmission electron microscopy (TEM) with energy dispersive spectroscopy (EDS) and X-ray diffraction were employed for the microchemical and microstructural analysis of the nanocrystalline $NbAl_3$ synthesized at the various processing conditions. These data will be discussed in conjunction with process variables.

2.1. Laser Ablation Apparatus

An apparatus to produce nanocrystalline materials by the laser ablation technique was originally developed for this research[22]. This system essentially consists of a high vacuum (HV) ablation chamber, vacuum system, laser optics and excimer laser. Fig. 2.1 shows the ablation chamber. This chamber is comprised of a powder-collector, a rotating target holder, a load lock, a stepper motor, and monitoring devices for temperature and pressure.

The main component of this laser ablation system is a rotating target holder with simultaneous rotational and linear translational motion under the high vacuum. The focused laser beam is so powerful that it will produce a highly localized hole on any

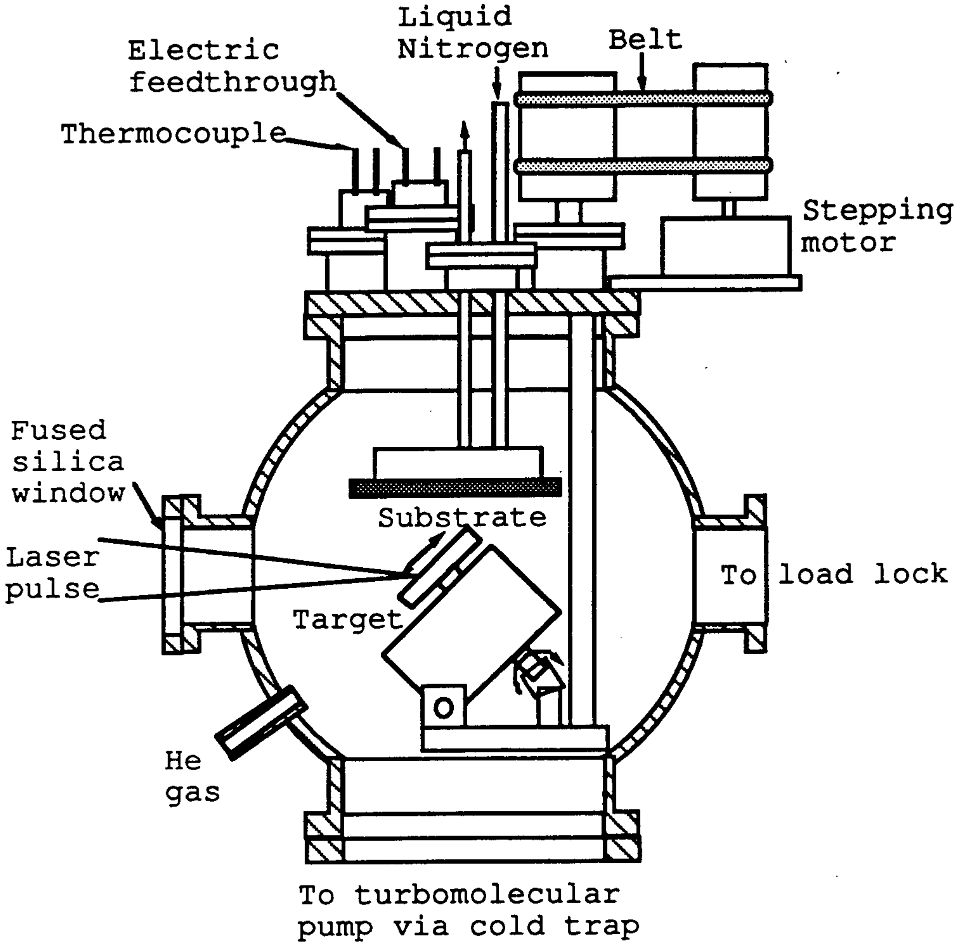

Figure 2.1. Schematic drawing of the ablation chamber.

stationary target materials in a very brief time. So, it is necessary to present a fresh target surface to the incoming laser beam at all the times, since excessive roughness in the irradiated target surface produces fluctuations of incident laser power density, which in turn leads to fluctuation of the composition of the vaporized materials.. In the present design, the target holder is rotated and simultaneously translated in a plane parallel to the target surface. The target motion is driven by a single external stepping motor which is controlled by a software program run on an 800 series controller from Velmex Inc. The top and side views of this device are shown in Fig. 2.2 (a) and (b). The mechanism is described below. The axial rod of the target table is connected through gears (not depicted) to a rotating rod which is connected to the stepper motor via a rotary vacuum feedthrough. The rotating motion of the target table is partially converted to translation through the use of a combination of worm gears and cams. Inside the worm gear box, the worm gear, which is attached to the rod of the target table, rotates with the target table. The worm gear transfers the rotational motion of the target table to the cams which are rotate about an axis at 90° relative to the rotation axis of the target table. The cams rotate very slowly at a speed determined by the number of gear teeth coupled to the worm gear and the translational pitch of the worm gear. The cams cause the target table sitting on the worm gear box to translate slowly along guide rails. The maximum translation distance is determined by the deflection of the rotating axis of the cam from its center.

The movement of this target holder can be uniquely tailored by the choice of rotation speed of the target table, number of gear teeth, pitch of the worm gear, and the deflection of the axis from the cam center. In the present case, the target table rotation is designed to be 2.4 rpm. The maximum translation distance is 6.35 mm and the target holder translates back and forth once every 20 rotations of the target table. The target disc of 28.58 mm diameter and 9.53 mm thickness sits on the holder. The vaporization path traced out by the laser beam on the target disc is a pair of spirals. The target is tilted at roughly 45° relative to the laser beam. Because translation occurs within a plane parallel to the target surface, the point where the laser beam touches the target surface is fixed in space (that is to say, in the lab frame. In the reference frame of the target, the laser beam appears, as noted, to trace out spirals.) This restricts the laser beam focus to remain on the surface of the target disc. This design, by minimizing target degradation, permits long continuous operation of the laser ablation experiment, producing sufficient materials for analysis from a single process run.

The powder collector block, made of Cu, was designed to be cooled to temperatures as low as liquid nitrogen boiling point (78 K) via a continuous flow of

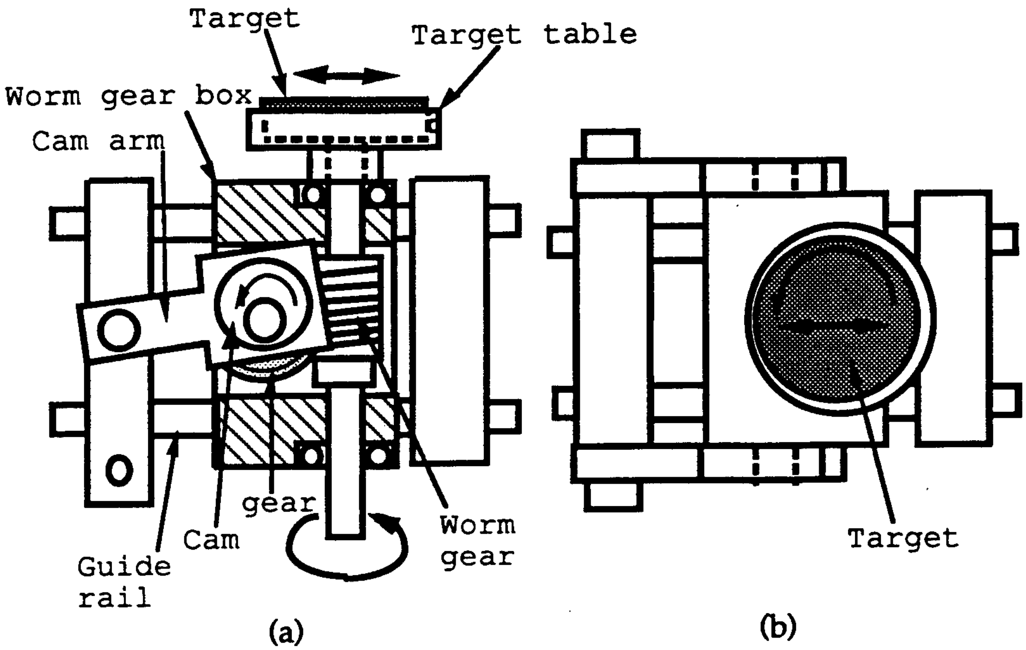

(a)

(b)

Figure 2.2. Schematic drawing of the target holder with mechanism of simultaneous rotation and translation. (a) side view and (b) top view.

liquid nitrogen through the block. The object of the liquid nitrogen flow is dual—to increase the collection efficiency and to suppress post-deposition grain growth. Fins within the chamber enhance the heat transfer for the effective cooling. The collection efficiency is thought to be enhanced partly by improving the sticking coefficient of the substrate, and partly by thermal gradients in the chamber leading to increased convection, thus improving transport of particles to the substrate. An aluminum substrate, onto which the nanocrystalline powders are actually deposited, is inserted into this block and can be removed from the chamber through the load lock without exposing the chamber to atmosphere. A thermocouple (type E, AWG#30), attached to the substrate via an electrical vacuum feedthrough, monitors the temperature of the cooled substrate. Other electrical connections, also supplied via the electrical feedthrough flange, enable the application of a DC bias between the target and the substrate. The back-filled He gas is introduced via a copper tube welded into a flange. The pressure within the chamber is monitored by two methods. A tungsten filament ion gauge measures pressures in the range 10^{-8}–10^{-3} Torr during evacuation before the experiment begins. A capacitance manometer (MKS Baraton 122B, MKS power supply PDR-C-1C), with a range of 0.01–100.00 Torr, is employed to monitor pressures during experiments, where the pressure ranges from 0.10 to 10.00 Torr.

2.2. Experiments

2.2.1. Production Experiments

The $NbAl_3$ target disc (99.5% pure, 28.58 mm diameter x 9.53 mm thickness) was hot-pressed from $NbAl_3$ powders by the powder manufacturer (Pure Tech. Inc., NY). The ablation chamber is first pumped down through a liquid nitrogen cold trap by a turbomolecular pump, achieving a base pressure of less than 2×10^{-7} Torr. The temperature of the powder collector reaches about 78 K several minutes after the liquid nitrogen flow is started. After closing the gate valve between the turbopump and chamber, He gas (scientific grade, 99.9999% pure) was back-filled into the chamber at the pressures of 0.10, 1.00, 10.00 Torr for the different process runs. Vaporization of the target material is driven by a KrF excimer laser (248 nm, Lambda Physik 201MSC) operating at a repetition rate of 50 Hz with pulse duration of 35 ns. The excimer laser beam is focused by a fused silica lens of 50 cm focal length; the focal spot is elliptical and 0.265 mm^2 in area on the target surface. The spot size was measured from burn pattern of the laser pulses. The pulse energies were varied between three levels, 270, 320, 370 mJ/pulse. The range of values for process variables (pressure and laser pulse energy) were based on preliminary experiments using the wider range of the values of the two variables. The values mentioned herein were selected as the most useful for determination of the effects of the process parameters. Processing experiments were performed at all nine combinations of the laser pulse energy and back-filled He gas pressure. Regarding the DC bias between the target and the substrate, it was observed that a DC bias in the range of up to ±500 V produced no significant effect on the processing. Thus, a DC bias was not applied in this study.

A portion of the synthesized nanocrystalline materials were collected on the aluminum substrate located at a position 22.35 mm above the laser spot on the target disc. This substrate is transferred through the load lock for subsequent characterizations. Enough materials for analysis can be collected after about 720,000 laser pulses. Collected powders on the substrate were scraped off the collector attached to the cold finger and removed from the process chamber, and then weighed for production rate measurements.

Sufficient materials for microstructure characterizations can be collected at only six laser energy/He gas pressure combinations—those conditions in which He gas pressures 1.0, 10.0 Torr were used. TEM and X-ray were employed to characterize the nanocrystalline powders produced under these conditions.

Special care is needed in handling the nanocrystalline alloys. Nanocrystalline powders have large surface area-to-volume ratio compared to bulk materials or the ordinary-size particles. The large relative surface area enhances the oxidation of the material since the degree of the oxidation is proportional to the surface area of the sample. Accurate material characterization by standard methods (TEM, X-ray, etc.) requires un-oxidized powders. All the sample handling and sample transfer from processing chamber to the analyzing instruments including a precision gravitational balance were conducted in a controlled argon atmosphere to minimize oxidation of the materials. Oxidation of the powders were reduced sufficiently that accurate examination of the powders became feasible.

2.2.2 Production rate and Ablation Rate

Collected powders at all the conditions were weighed using a precision gravitational balance (Perkin-Elmer, ±0.1 mg for 1000 mg range) in argon atmosphere to reduce the oxidation of the materials. The ablation rate was determined from the target weight loss before and after each processing experiment employing the balance (Mettler AE163, ±0.1 mg for 160 g range).

2.2.3. Microstructural and Microchemical Analysis by TEM

TEM image was taken from a thin area using a Philips 420 electron microscope operating in the bright field mode at 120 kV. The specimen was carefully transferred to the TEM specimen chamber under an argon atmosphere. Selected area diffraction pattern of the same area as the TEM image was also taken to determine the crystal structure. For the measurement of a mean diameter of the nanocrystalline powders, TEM photographs (magnification=164,000) were used to measure the particle diameters. About 500 particles were sampled randomly from a particular sector on the TEM picture of powder produced under each process condition. The powder diameters then were carefully measured. The obtained data were processed to draw histograms and obtain statistical data on the size distributions, i.e. mean diameters and variances.

Microchemical analyses of the powders were performed using transmission electron microscopy (TEM, Philips 420) equipped with energy dispersive spectroscopy (EDS). EDS was carried out using s Si(Li) detector equipped with an ultra-thin window and Be window removed, permitting the detection of peaks of light elements (oxygen here). The take-off angle was 33.5°.

The chemical composition in the Nb-Al nanocrystalline powders were determined from characteristic X-ray intensities for each element using the standard quantitative analytical technique for thin specimens. The K_{AB}-factor which relate the concentration ratios to the intensity ratios of EDS of the different elements A and B were determined by analyzing a thin area of a stoichiometric $NbAl_3$ standard[24].

2.2.4. X-ray Diffraction

XRD patterns for the present experiments were taken at room temperature using a Rigaku XRD with DMAXIIIA controller. The Rigaku XRD is equipped with a monochromatic CuKa X-ray source filtered by a graphite monochromator in front of the detector and operated at 45 kV and 28 mA. The controller allows automatic operation of X-ray diffractometer. X-ray data acquisitions were automatically done by the DMAXIIIA controller and simultaneously data were stored on the memory disc. Samples were scanned once between 2q = 2° and 82° at a scanning speed of 1° min^{-1} in 2q/q reflection mode.

2.3. Results and Discussions

2.3.1. Production Rate and Ablation Rate

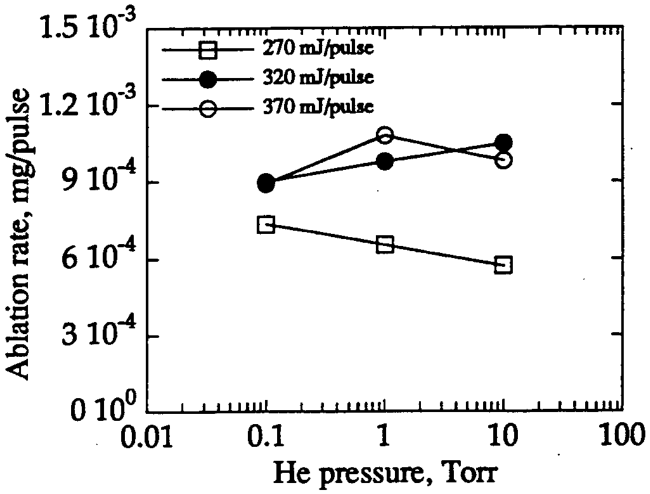

Figure 2.3. Ablation rate as a function of He back-filled pressure for different laser pulse energies.

Ablation rate is the mass evaporated from the target per laser pulse. The ablation rate as a function of the He back-filled gas pressure at each laser energy level is shown in Fig. 2.3. This shows that the ablation rate is relatively insensitive to the changes in He pressure. It is also shown that the ablation rate is not a linearly increasing function of laser pulse energy. It rises from the 270 mJ/pulse to 320 mJ/pulse, but remains almost unchanged from 320 mJ/pulse to 370 mJ/pulse. Stafast and Przychowski measured the evaporation rate of various pure metals and ceramics at the gas pressure and reported the similar behavior[13]. Miyamoto, Ooie, Hirota and Maruo interpreted this phenomena by measuring the transmissivity of laser beam through the laser induced plasma plume[25]. They concluded that at later times within the laser pulse, the plasma created by material ablated at earlier times strongly absorbs the laser beam, thus saturating the ablation rate. This suggests that there exists an efficient range of laser pulse energies for ablation of the material.

Weights of the collected powders synthesized at the various conditions can be used to reflect the amount of powders produced at each processing condition and are useful to determine the optimum conditions for the maximum powder yield. Fig. 2.4 shows the weight of produced powders as a function of the process variables, i.e. laser pulse energy and He pressure. No detectable nanocrystalline powders were produced using He pressure of 0.10 Torr for any laser pulse energy. In fact, in prior experiments it was observed that a thin film formed on the substrate at the pressure below 0.10 Torr. This means that the condensation of gas atoms into stable nanoparticles requires the surrounding inert gas pressure to be above some threshold value. An interesting fact is that powder production rapidly increases with an increase of He pressure up to 1.00 Torr and after this it decreases slowly with further increase of He pressure. Production rate is strongly dependent on the gas pressure. This pressure dependence of the production rate is in contrast to the evaporation rate which is relatively unchanged over the pressure change.

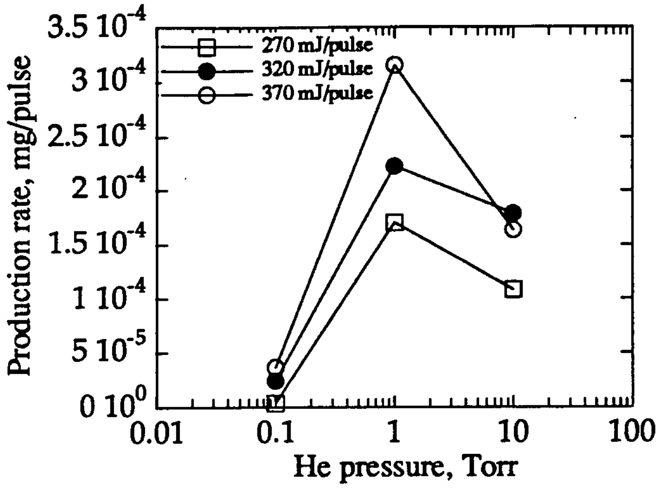

Figure 2.4. Production rate as a function of He back-filled gas pressure.

In ablation processing, the atoms evaporated by the laser pulse leave the target with large kinetic energies. Then, they collide with He gas atoms as they move, shedding kinetic energy rapidly and eventually condensing to form the fine nanocrystalline grains. Thus, the nucleation process is related to the both the background pressure of the inert gas and the gas dynamics of the evaporated metal atoms. The optimum conditions for maximizing the production rate depends on them.

2.4.2. Microstructures by TEM

Typical TEM micrographs and electron diffraction of nanocrystalline powders are presented in Fig. 2.5. Fig. 2.5 shows the TEM micrograph of powder from the process run at laser pulse energy of 370 mJ and back-filled He pressure of 1.00 Torr. This photograph shows that the individual particles are spherical and well isolated from each other, and also that particle size is very homogeneously distributed. An electron diffraction pattern of the powders reveals a broadened diffraction ring due to the effect of the small particle size. Crystal structure was confirmed to be $NbAl_3$. Randomly distributed sharp white spots are due to some slightly larger particles that satisfy the Bragg condition.

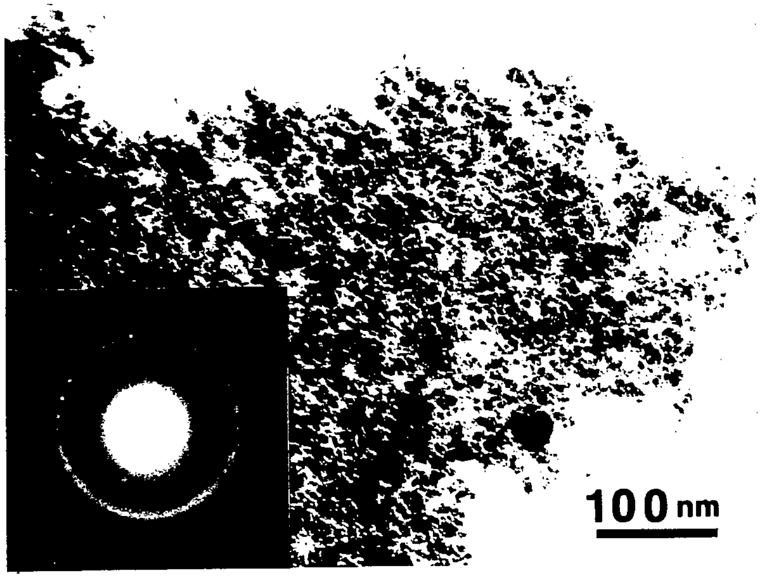

Figure 2.5. Transmission electron micrograph(a) and electron diffraction pattern(b) of nanocrystalline $NbAl_3$ synthesized at 370 mJ and 1.0 Torr.

Size distributions of nanocrystalline powders were obtained from TEM micrographs. Fig. 2.6 shows typical size histograms of nanocrystalline powders synthesized under the same processing conditions as the powder in Fig. 2.5. Average particle diameter is 6.2 nm and variance of the distribution is 2.4. The size distribution appears to be very narrow. Fig. 2.7 summarizes the data from the histograms which shows the correlations between the mean particle diameters and the processing variables. It is obvious that particle size increases and distribution width broadens as He pressure increases from 1.00 Torr to 10.00 Torr. Irrespective of the laser pulse energy, the particle diameters increase as He pressure increases. This graph also shows that the laser pulse energy has a strong influence on the particle diameter, i.e. particle diameter decreases by half as the laser pulse energy increases from 270 mJ to 320 mJ. However, no noticeable change in particle diameter was seen as the pulse energy increased from 320 mJ to

370 mJ. Fig. 2.8 shows the change in variance of the size distributions as a function of the He pressure and the laser pulse energy. Variance can be thought as a measure of the broadness of the size distribution. The smaller the value is, the narrower the distribution. It is manifest that the size distributions get broader as the He pressure increases for each value of the laser energy. The effect of He pressure on the variance is large. The laser pulse energy has the same effect at 10.00 Torr. However, the effects of the laser pulse energy at 1.00 Torr are very small. These effects of processing parameters (laser pulse energy and He pressure) on the size distributions are consistent with the results of observations of the TEM micrographs. The ablation rate increases from 270 mJ to 320 mJ, but remains unchanged from 320 mJ to 370 mJ. These results showed that the net effect of the laser pulse energy of 320 mJ is the same as that of 370 mJ on the yield of nanocrystalline powders. That is , the net effect of the laser pulse energy of 320 mJ on the material characteristics can be expected to be the same as that of 370 mJ. This results of the ablation rate are consistent with the trend of the present data of the particle size as a function of the laser pulse energy.

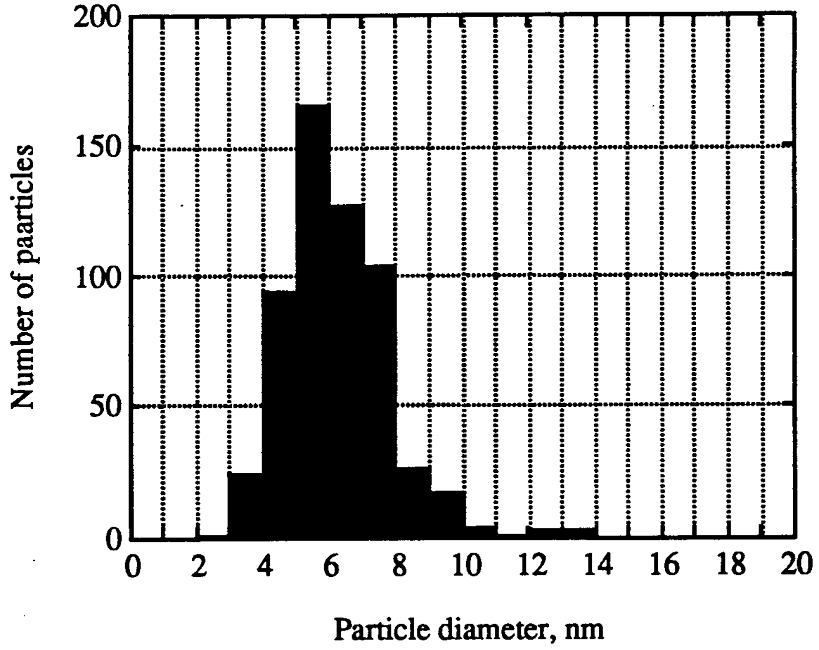

Figure 2.6. Size distribution for $NbAl_3$ particles synthesized at 370 mJ and 1.00 Torr. Mean diameter=6.2 nm, variance=2.4.

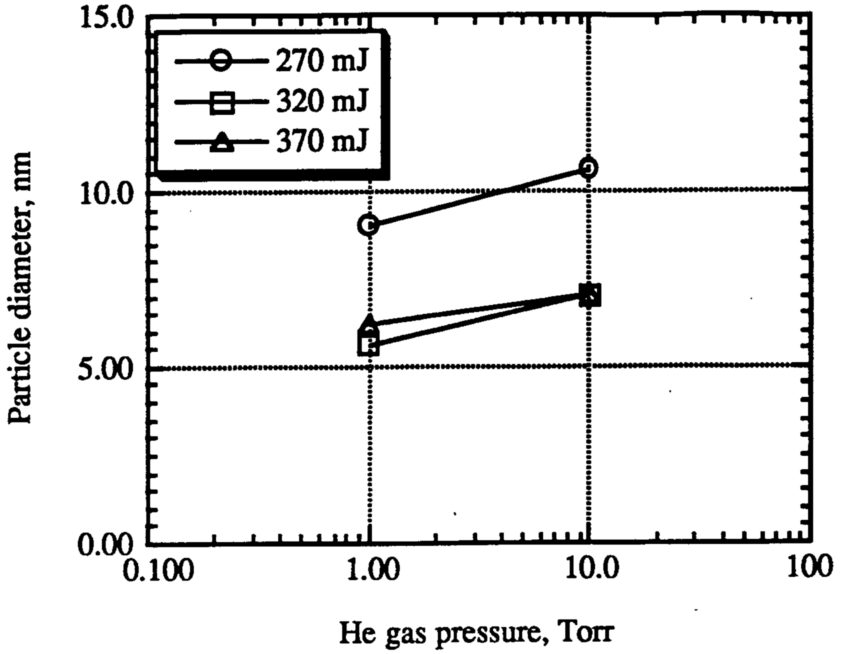

Figure 2.7. Particle diameter as a function of laser pulse energy and back-filled gas pressure.

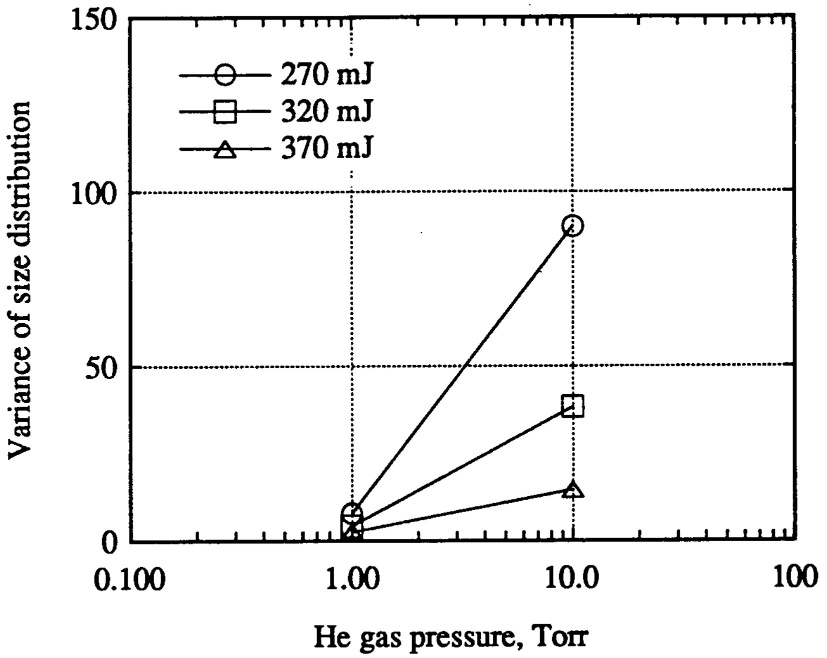

Figure 2.8. Variances of finer particles' size distributions as a function of laser pulse energy and back-filled He gas pressure.

The critical radius, r_{crit}, for the condensing particle in equilibrium with the vapor is derivable from thermodynamic considerations and may be expressed:

$$r_{crit}=2gV_{mol}[RT\ln(P_v/P_o)]^{-1},$$

where g is interfacial energy, V_{mol} is the molar volume, R is the gas constant, and P_v/P_o is the supersaturation ratio, that is, the vapor pressure divided by the equilibrium vapor pressure at absolute temperature T[26]. Higher laser pulse energies result in the vaporizing species having larger kinetic energies. This, in turn. creates an increase in the supersaturation ratio. Therefore, the critical radius r_{crit} of the particle decreases. Back-filled He gas reduces the kinetic energy of the vapor by collisional interactions and therefore reduces the supersaturation. This explanation is compatible with the present data of the dependence of the particle size distributions on the laser pulse energy and the back-filled pressure. Hence, the formation of the fine particles observed by TEM is due to the gas condensation of laser ablated vapor.

2.3.3. Chemical Analysis by EDS

Chemical analysis data shown here were taken by employing the EDS apparatus attached to the TEM. A typical EDS spectrum of the powders synthesized at 1.0 Torr and 370 mJ is shown in Fig. 2.9. A Cu peak seen at intermediate energy arises from the presence of the Cu grid which serves as a specimen holder for the powders and also from the pole piece of the TEM. The small peak located at an energy 1.74 keV below the copper peak is an artifact due to fluorescence of the Si detector excited by the Cu radiation. It does not come from the powders. These two peaks were confirmed to be artifacts by using a hole count technique in which EDS data was taken while the electron beam passed through an empty region of the grid instead of the sample. The atomic ratio of Al to Nb of the nanocrystalline powders synthesized under each processing condition was calculated from the integrated intensities of Al and Nb peak after background subtraction. Fig. 2.10 summarizes the relationships of atomic ratio and the processing parameters. It is noteworthy that the exact 3 to 1 stoichiometric composition of $NbAl_3$ was preserved in the powders synthesized under the conditions of laser pulse energy 270 mJ and 10.00 Torr. The atomic ratio of Al/Nb decreases from this congruent stoichiometric composition with increasing laser pulse energy and decreasing He pressure. Larger deviations from congruent composition are seen with changes of pressure than of the laser pulse energy. It is also noted that the atomic ratio does not change as the laser pulse energy increases from 320 mJ to 370 mJ. A similar non-effect the consideration of the particle diameter variation. This can be understood in the same context as the explanation for the lack of change in the ablation rate data over these energies [22].

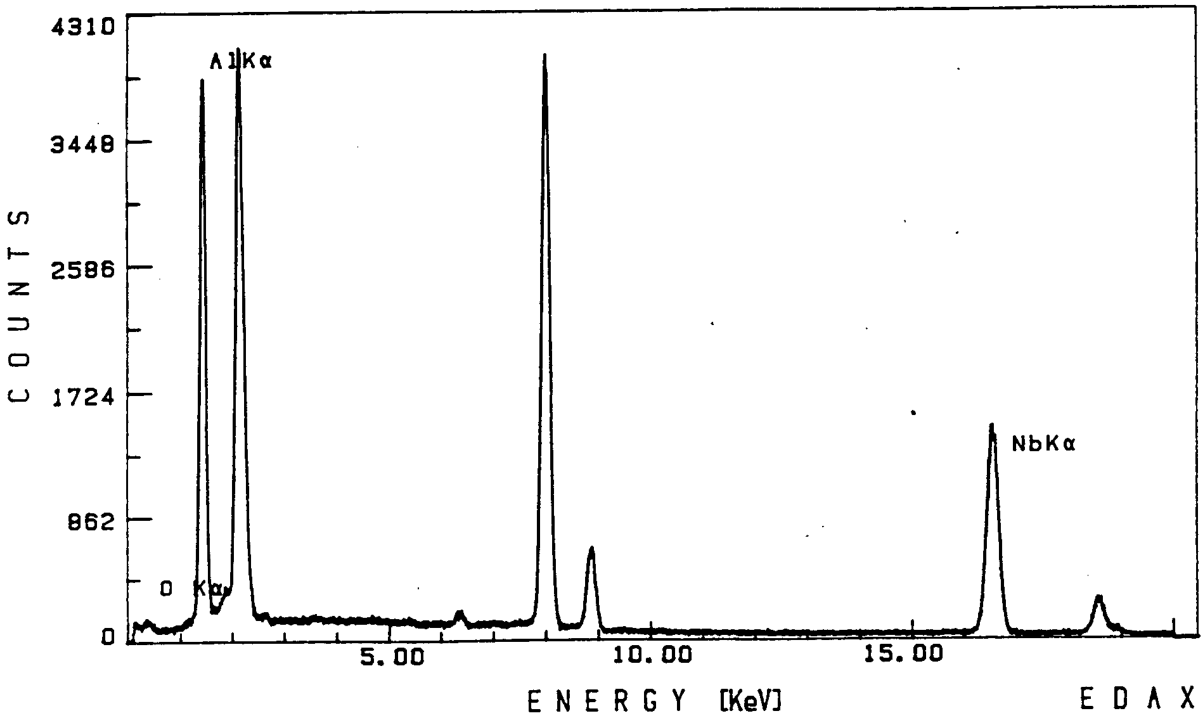

Figure 2.9. Energy dispersive spectroscopy (EDS) of nanocrystalline $NbAl_3$ synthesized at 370 mJ and 1.0 Torr.

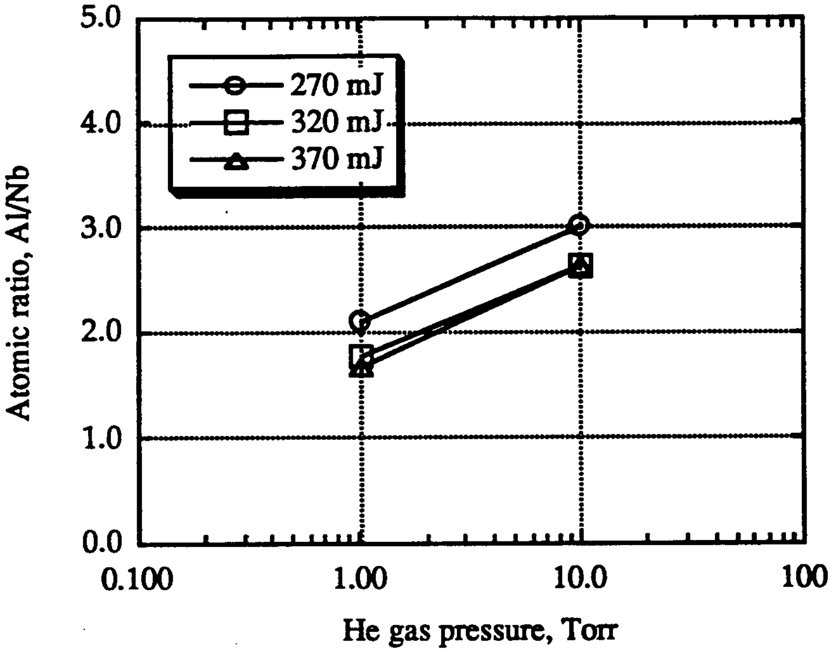

Figure 2.10. Atomic ratio(Al/Nb) of nanocrystalline particles as a function of laser pulse energy and He gas pressure.

In general, the target material was irradiated by the laser beam with enough power to evaporate congruently, so that the composition of the laser-induced plasma is unchanged from the composition of the target material and thus the composition of the material synthesized by laser ablation can be expected to be equal to the target composition[27]. However, present data shows a larger Al deficiency (as compared to target stoichiometry) as either laser power increases or the ambient He pressure decreases. There are several possible mechanisms responsible for this anomalous Al deficiency: (i) selective evaporation due to different evaporation rates of the components Nb and Al from the target surface for low energy incident beams[28], (ii) different sticking coefficients of the components Nb and Al during the nucleation and growth of nanocrystallines, (iii) preferential sputtering of the components Nb and Al from the nanocrystalline particles by the impact of the high energy ablated species[29]. The first effect arises from the irradiation of the low energy incident beam. However, the composition of the particles synthesized at 270 mJ and 10.00 Torr was congruent and those at the higher energy are all Al deficient. Therefore, the laser energy is thought to be large enough to evaporate the target material congruently. Hence, this selective evaporation effect seems unlikely. There are no available data on the sticking coefficients of the components Nb and Al on the nanocrystalline particles. Regarding the third mechanism, the kinetic energy of the ablated species are positively proportional to the laser pulse energy. The sputtering power increases positively as a function of the kinetic energy and therefore laser pulse energy. Generally, Al atom can be more easily sputtered than Nb atom. The back-filled He gas has the effect of reducing the kinetic energy of the ablated species, which are the sputtering agents, by collisional interactions and therefore decreasing the sputtering power. This explanation is compatible with the present compositional dependencies on both laser pulse energy and back-filled gas pressure. However, some of newly ablated high energy species also stick on the particles and play a part in determining the sputtering effect. It is difficult to identify unambiguously the responsible mechanisms with the available data. Also, there may be other mechanisms contributing to this Al deficiency from stoichiometric congruence.

2.3.4. X-ray Diffraction

Fig. 2.11 shows a typical X-ray diffraction pattern of the nanocrystalline powders. Indexing of the peaks reveals that the crystal structure is $D0_{22}$ of $NbAl_3$. Nanocrystalline powders synthesized at all other conditions showed the same diffraction patterns and were identified to be $NbAl_3$ structures. According to the chemical analysis data, all other powders except the one synthesized at 270 mJ and 10.00 Torr had compositions different from the stoichiometric composition of 3 to 1 of Al/Nb. This fact suggests that a nonequilibrium process occurs during the nanocrystalline formation from the vapor phase. This can be understood by the fact that there is no phase found near the $NbAl_3$ line composition in the phase diagram. Lattice constants of the nanocrystalline powders at all processing conditions are found to belong to ordinary $NbAl_3$ crystal.

XRD data were also used to investigate the particle size distributions of powders as a function of the processing variables. Each Bragg peak of the $NbAl_3$ nanocrystalline powders can be seen to broaden at its foot. This fact suggests that each peak is actually a composite peak comprising one relatively narrow and one low, broad peak. The broad pedestal may be explained according to the Scherrer's small size effect, in conjunction with a bimodal size distribution of finer and coarse particles. The TEM micrographs already revealed two distinct grain sizes and is consistent with the present observation of the XRD results. To investigate the bimodal sizes of finer and coarse particles, the (112) Bragg peak was fitted with two Cauchy functions after background subtraction. Fig. 2.12 shows the original (112) composite peak and two fitted curves from the XRD data of Fig. 2.11. Then, the full width at half maximum of the pure diffraction profile (b) of each curve was calculated after instrumental broadening corrections to determine the two different particle sizes in the mixtures of finer and coarse powders[30, 31].

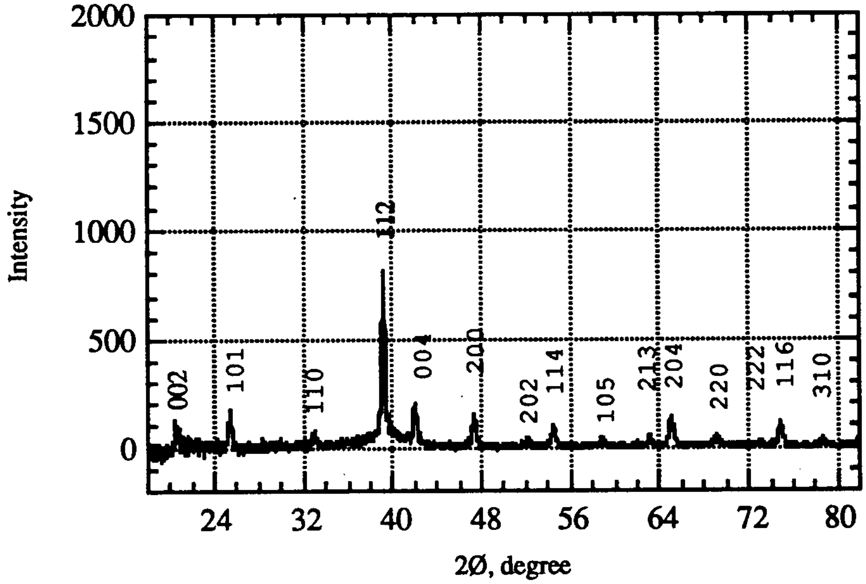

Figure 2.11. X-ray diffraction pattern from nanocrystalline $NbAl_3$ synthesized at 370 mJ and 1.0 Torr.

The Scherrer formula used in the present study which correlates the particle size with the FWHM of the Bragg peak is expressed by the following equation[30];

$$D = \frac{K\lambda}{\beta\cos\theta} \quad \text{(Scherrer formula)}$$

where

$K = 0.94$,

β = FWHM of the diffraction peak,

D = effective thickness in a perpendicular to the reflecting plane,

λ = wave - length of X - radiation,

θ = the Bragg angle.

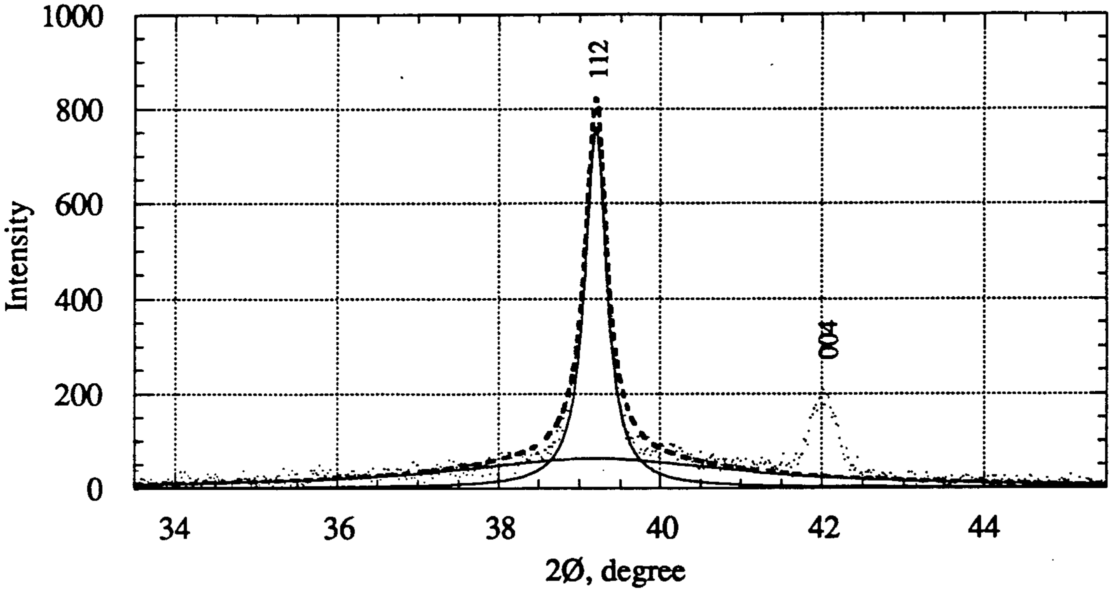

Figure 2.12. Curve fitted X-ray peak (112) of nanocrystalline $NbAl_3$ synthesized at 370 mJ and 1.0 Torr. Broken line is the sum of the two solid fitting curves.

In the manner described above, FWHM values of two pure diffraction peaks, i.e. one sharp and one broad were calculated from one composite peak. From these widths, particle size, D, can be directly calculated by Scherrer's formula. Information on the bimodal particle size distributions has been obtained. The volume ratios of fine powders to coarse powders are obtained from the ratios of the integrated intensities (i.e., the area under the fitted curve) of the broad and sharp peaks. The results obtained by the above analysis methods will be discussed in connection with the processing parameters in a later section.

Fig. 2.13 shows the relationships between the size of finer particles and the pressure of the ambient gas (He) at the laser pulse energies, 270 mJ, 320 mJ and 370 mJ. These size data were calculated from analysis of the broader of the two fitted curves of each bimodal composite peak indexed (112). This data shows that the size of the finer particle decreases as the gas pressure decreases at every laser pulse energy and also that it decreases as the laser pulse energy increases from 270 mJ to 320 mJ, but remains unchanged from 320 mJ to 370 mJ. Particle sizes in this range fall in about 2–3.5 nm. The XRD data just described shows that the effects of the gas pressure and the laser pulse energy on the particle size agree with the TEM results. However, particle sizes obtained by the XRD analysis are observed to be smaller than those by the TEM analysis.

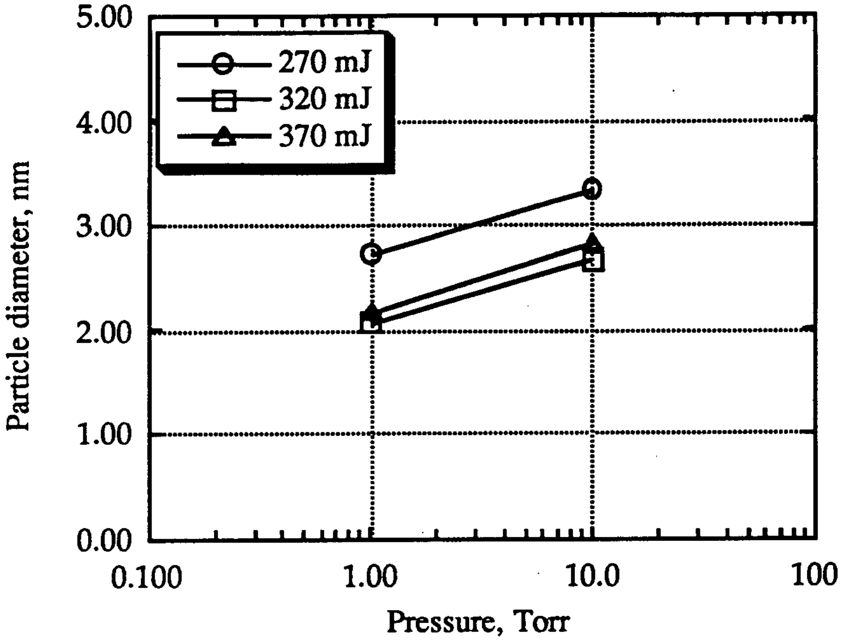

Figure 2.13. Finer particle diameter as a function of laser pulse energy and back-filled gas pressure. The data was taken by X-ray analysis.

Here, it is advisable to know the experimental limitations of the XRD and TEM methods. XRD covers a broad irradiated area of the specimen containing countless number of irradiated particles, and gives us overall information of that area. On the other hand, TEM gives us the precise and visual information of a very small area on the micron scale. For the statistical analysis by TEM, we focus only on the very small particles, although we can see only one big particle which makes no significant contribution to the statistical analysis. For the range of the sizes encompassed by the present bimodal distribution, analysis of TEM data can only observe a statistically significant sample for the finer particles . For this reason, comparison of X-ray data and TEM data will be made only on the finer particles.

Difference of particle size values between XRD and TEM experiments have also been reported by other researchers[32]. Berry studied the shape of the XRD lines on magnesium oxide (MgO) and reported that the particle sizes measured by TEM appeared to be two to three times larger than the sizes determined by XRD. The present results showed the same order of the difference as Berry's results. Possible reasons for this mismatch are related to material imperfections, namely (a) coherent domains and (b) surface disorders. These crystal imperfections also cause peak broadening, and therefore modify the peak shape.

Small angle boundaries originating from dislocations subdivide the original particle into small coherent domains. These domains sometimes have enough disorientation with respect to one another to cause incoherent scattering. Thus, the domains in one particle act as very small crystals. X-ray sees the domains not the particle[33]. Almost any grain can be thought to have defects acting like dislocations. Thus, this reason is the most plausible.

It is well-known that surface atoms on the particle have different chemical states from inside the particle and form a randomly-oriented crystal structure. The surface layer doesn't scatter X-ray coherently, and, thus, the particle will be seen to be smaller by XRD. Since the surface-to-volume ratio of nanocrystalline particle is very large, this may also explain the difference in size.

Fig. 2.14 shows the relationships between the sizes of the coarse particles and the processing parameters. Size data was taken from analysis of the corresponding sharper peak of two fitted curves of the (112) peak. Particle size decreases as the gas pressure decreases at all the laser pulse energies. The effect of the gas pressure on the size of the coarse particles are shown to be the same as that observed in the finer particles. A significant effect of the laser pulse energy on size is not found in the present experiment. The sizes of the coarse particle are in the range of 70 to 150 nm depending upon the gas pressure.

Fig. 2.15 shows the volume ratio of fine particles to coarse particles. It is found that more fine particles were produced at 1.00 Torr than at 10.00 Torr irrespective of the present range of the laser pulse energy. About 60% of whole powders are classified into finer powders at 1.00 Torr.

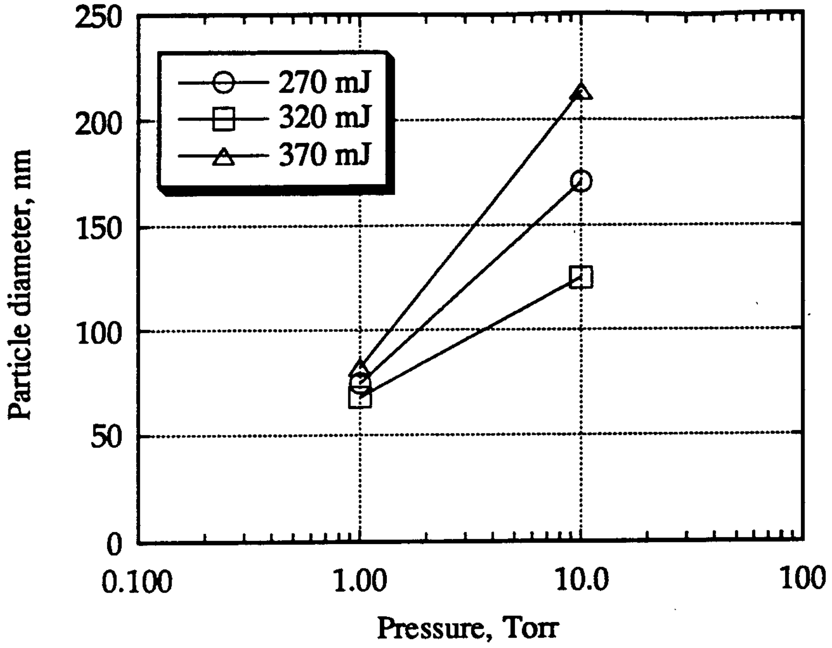

Figure 2.14. Coarse particle diameter as a function of laser pulse energy and back-filled gas pressure. The data was taken by X-ray analysis.

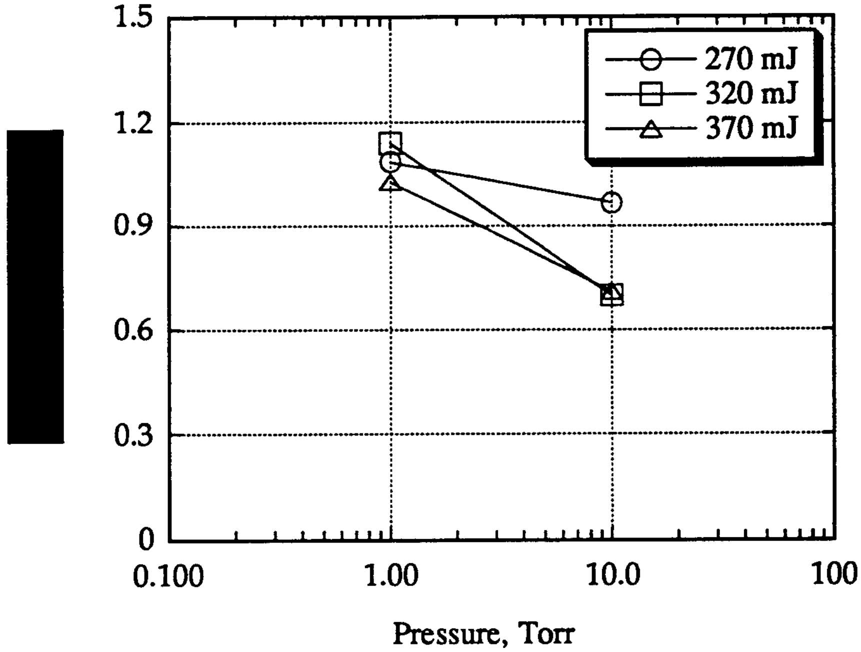

Figure 2.15. Volume ratio of finer particles to coarse particles as a function of laser pulse energy and back-filled gas pressure. The data was taken by X-ray analysis.

It is evident that the two distinct particle size distributions arise from different mechanisms of the particle formation. As discussed earlier, the finer particles are formed by the gas condensation of the laser induced vapor. The formation mechanism for the coarse particles may be due to the ablation of the loosely attached target flakes[34] and explosion of the subsurface target material due to the subsurface superheating[35].

2.4. Powder Synthesis: Conclusions

Nanocrystalline $NbAl_3$ powders were synthesized by the new processing technique with various processing conditions. The property/structure/processing relationships of this new processing were understood through a series of characterizations of nanocrystalline powders synthesized at systematically-varied processing conditions. There is no doubt that these data play a fundamental role in controlling the process and developing this process further to get nanocrystalline powders of desired properties. Production rate and ablation rate were obtained at various processing conditions. The following are the results revealed by the present investigation.

It has been found that maximum efficiency of the production rate is most strongly dependent on He pressure. This suggests that the processing variable should be carefully chosen to obtain the nanocrystalline materials effectively.

It was revealed that the synthesized nanocrystalline powders were a mixture of finer and coarse particles both of which have $D0_{22}$ crystal structure. The volume ratio of the two different size distributions are dependent on both laser pulse energy and back-filled gas pressure. Sizes of both finer and coarse particles were also functions of these processing parameters. The trends of sizes and chemical compositions of finer particles were similar and were correlated with ablation rate especially in the laser energy dependency.

2.5. $NbAl_3$-Al Multilayer Microlaminate Films

It was noted that the laser ablation system at low pressures (e.g. below 1 Torr) yielded nanocrystalline-grained thin films, rather than powders. This suggested a different approach to maintaining the strength and oxidation resistance of $NbAl_3$ while gaining the ductility of a metal. A number of experimental studies[36, 37] have shown that a film composed of alternate thin layers of ductile and brittle materials can enhance ductility of the brittle material while retaining its strength. Theoretical work[38, 39] suggests that this enhancement, and particularly the inhibition of crack propagation, in such multilayered structures becomes much more effective as the individual layer thicknesses decrease. The difficulty in producing such films rests in maintaining stoichiometry in the thin intermetallic layers, and more generally in precise control of the individual layer thicknesses between the ductile and brittle materials. The ablation system described herein has a demonstrated capability to grow thin films of intermetallics. Furthermore, the fine grain structures of these films should possess improved ductility in their own right, as well as improving adherence to a different-structured ductile layer. Finally, laser ablation's ability to produce vapor plumes in materials with vastly different melting/boiling points with no change in process parameters makes it an ideal evaporation source for such heterogeneous deposition applications. With these considerations in mind, we endeavored to demonstrate the feasibility of interleaving ductile aluminum layers and $NbAl_3$ layers resulting in a $NbAl_3$-Al multilayered film. the results of these proof-of-concept experiments are described below.

2.5.1. Multilayer Fabrication

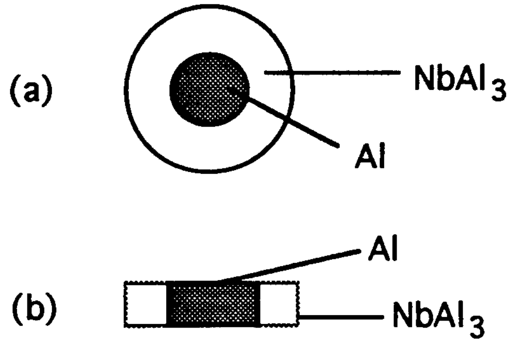

Figure 2.16. Compound $NbAl_3$/Al Target. (a) Top View. (b) Side View.

The KrF excimer laser (LambdaPhysik, EMG201 MSC) with 248 nm wavelength, 270 mJ energy, and 10 Hz pulse repetition rate is focused to a spot size 2.6 mm^2 on a disc-shaped $NbAl_3$ target (Al inside, refer to Fig. 2.16). The target (diameter ~2.6 cm) was rotated(16 rpm) and moved back and forth in one direction, alternately bringing the $NbAl_3$ and Al regions under the focused laser spot, thus depositing alternating layers of the two materials. The base pressure was approximately 3×10^{-7} Torr and a continuous flow of He gas at a constant chamber pressure of 100 mtorr was maintained during deposition. An unetched silicon substrate with amorphous surface structure was located 4 cm from the target. Deposition was performed for 90 minutes and the substrate was either cooled down with liquid nitrogen or was at ambient temperature during deposition.

Laser pulse energy (either 270 mJ or 290 mJ), substrate temperature (either liquid nitrogen cooled or room temp.), and He gas pressure(0, 100 mtorr, 200 mtorr) were varied to produce films with better nanocrystalline microstructure.

Amorphous structure of the deposited films was observed for all process runs in which no backing He gas was used. This result corresponds to published data[40-42].

After this verification, He gas was used during deposition to produce films with nanocrystalline grain size. Fig. 2.17 shows that nanocrystalline phase begins to form with laser energy of 270 mJ, 100 mTorr He pressure and cooling a substrate with liquid nitrogen. In these runs, we cooled substrate with liquid nitrogen to prevent grain growth beyond nanosize. After producing this film we used higher He gas pressure (200 mTorr) during deposition to get more apparent nanocrystalline structure(Fig. 2.18). Average grain size was roughly 30 nm and the film appeared very homogeneous.

Figure 2.17. Nanocrystalline film, produced with 270 mJ laser energy, 100 mTorr of He while cooling substrate with liquid nitrogen.

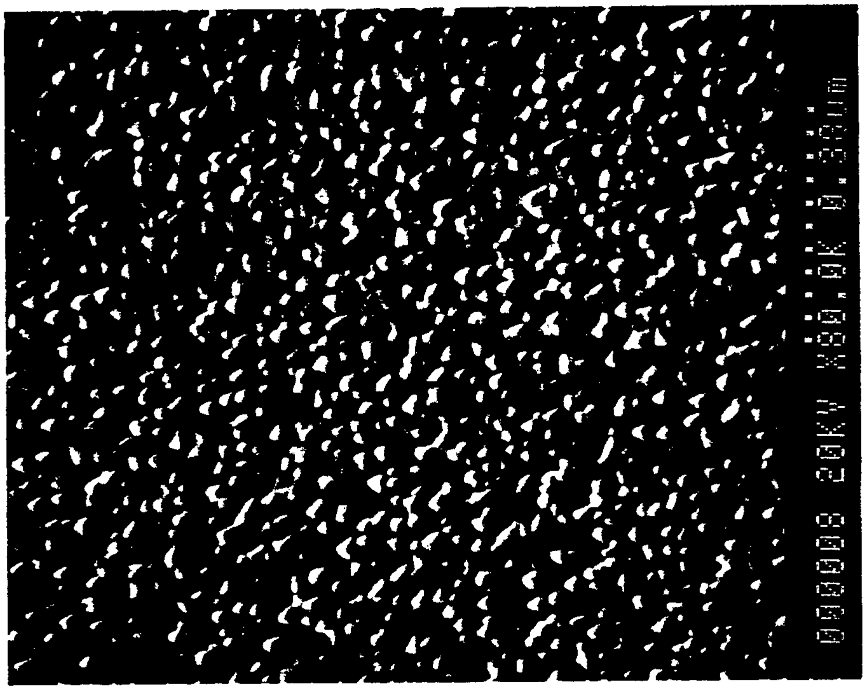

Figure 2.18 Nanocrystalline film , produced with 270 mJ laser energy, 200 mTorr of He while cooling substrate with liquid nitrogen.

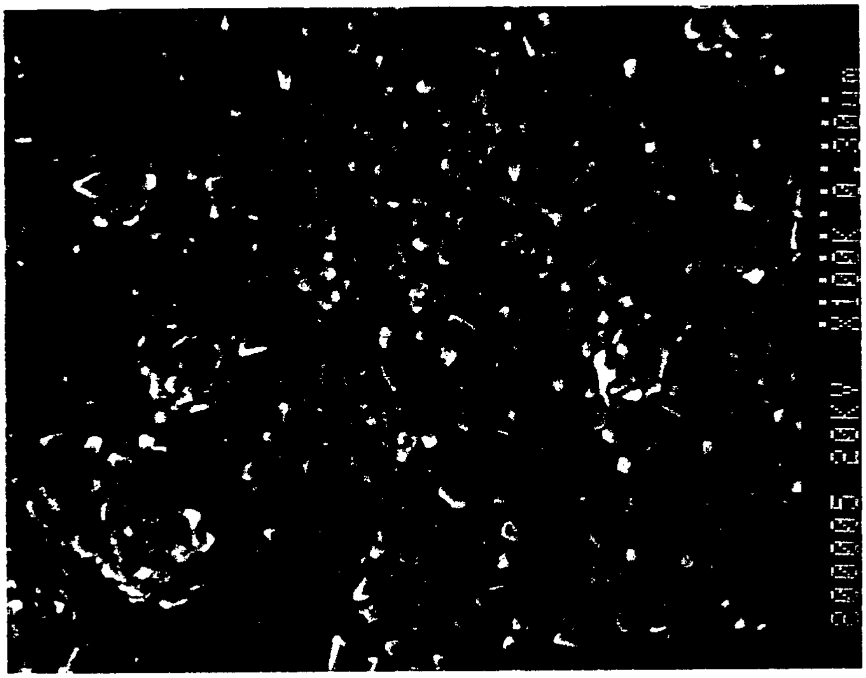

Figure 2.19. Platelet nanocrystalline film, produced with 270 mJ laser energy, 200 mTorr of He at ambient temperature.

Figures 2.18 and 2.29 show the microstructure of two films produced under identical conditions with the exception that no liquid nitrogen cooling of the substrate was used for the film in Fig. 2.19, e.g. deposition occurred at ambient temperature. The actual substrate temperature is likely much higher than room temperature due to high plume temperature (> 3000 K). The film produced exhibits a platelet microstructure which corresponds to Blocher's theory[23] (Table 2.1), and Tucker model[43] (Fig. 2.20(d)).

EFFECT OF INCREASED SUPERSATURATION ↓

Epitaxial Growth
Whiskers
Dendrites
Polycrystals
Fine Grained Polycrystals
Amorphous Deposits
Gas Phase nucleated "Snow"

↑ EFFECT OF INCREASED TEMPERATURE

Table 2.1. Influence of temperature and supersaturation in deposition of condensed materials. (Blocher 1974)

COATINGS: PHYSICAL & MECHANICAL PROPERTIES

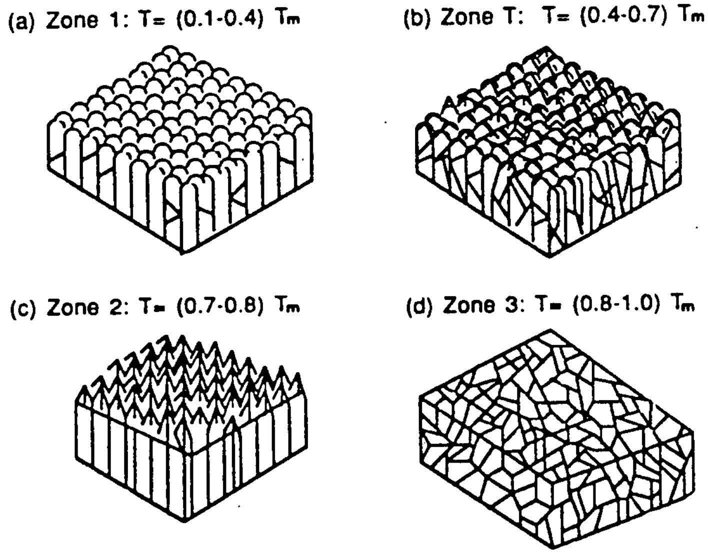

Figure 2.20. Structural Zones in Vacuum Condensates (Mochivan & Demchischin categorization; Zone T - Tucker Model).

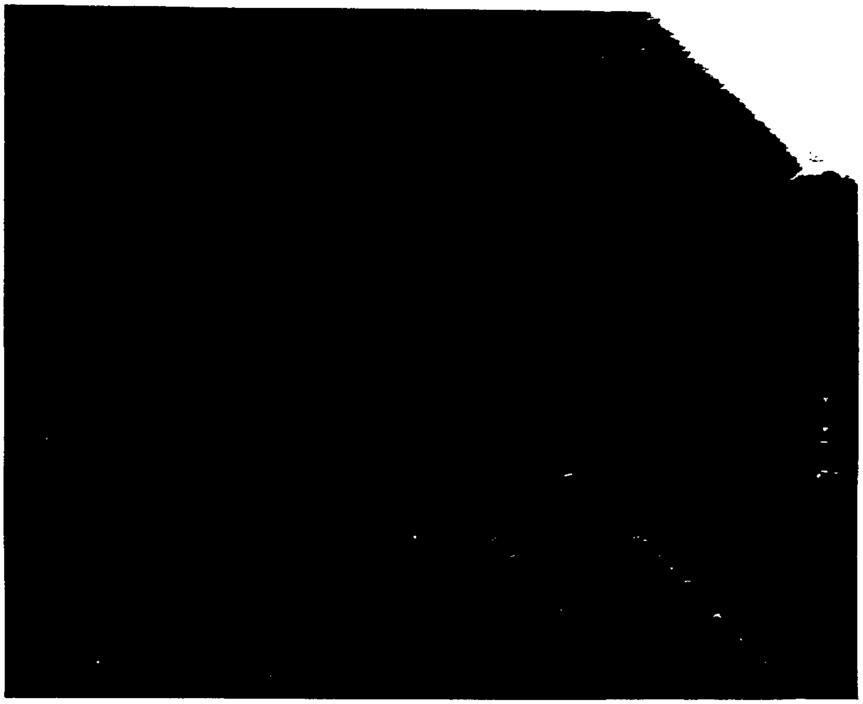

Figure 2.21. Cross section of Al-$NbAl_3$ microlaminated film.

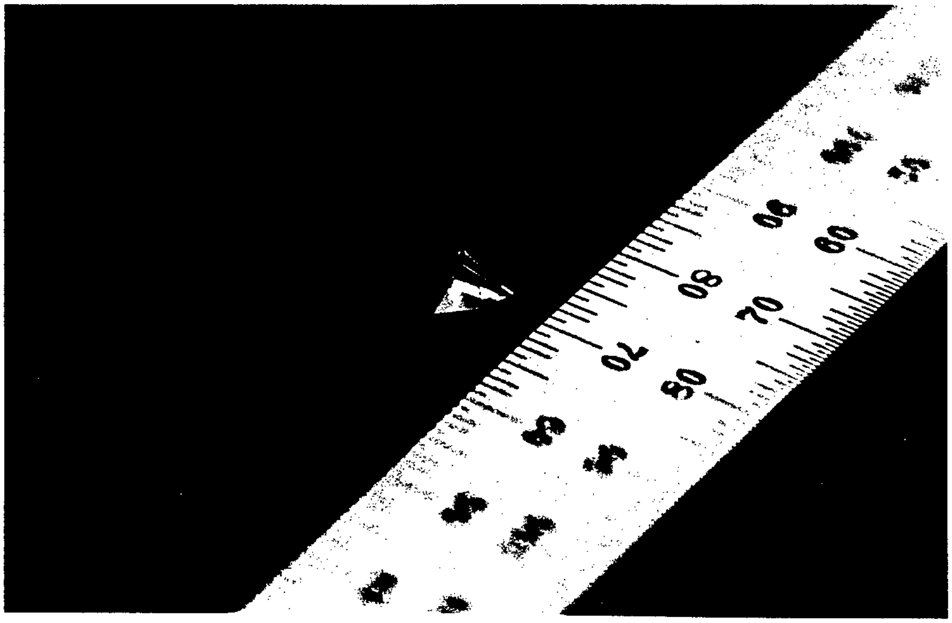

Figure 2.22. Photograph of a piece of $NbAl_3$-Al film which shows ductility of the film.

Fig. 2.21 shows a cross section of a film in which each Al and $NbAl_3$ layer may be distinguished by image contrast. According STEM results, the brighter layers are Al and darker layers are $NbAl_3$. Both parts possessed stoichiometric composition. We deposited an Al layer for 180 sec and a $NbAl_3$ layer for 300 sec which result in 8 nm and 64 nm thickness of each layer.

The ratio of deposition time between Al and $NbAl_3$ was altered to 220 sec: 260 sec to thicken the Al layers and the resultant film appears to be very ductile. A photograph of this film was taken after breaking the substrate and Fig. 2.23 exhibits the excellent ductile property of the film.

2.5.2. Plans for Future Work

We will control relative thickness ratio of Al and $NbAl_3$ layers, which will influence the hardness of the film. Then ductility of the film will be measured through bending testsing a film deposited on a substrate with well-characterized mechanical properties. The nterface between layers also will be observed with TEM(Transmission Electron Microscope) to improve mechanical properties of the film.

- Epitaxially grown microlaminated films will be produced, which are expected to have better mechanical properties.

- Deposition procedure will be diagnosed with laser spectroscopy to characterize time evolution of both temperature and expansion velocity of the plume and the plume density (atom or molecule) will be also analyzed during laser ablation.

Chapter 3 Optical Diagnostics

Laser absorption spectroscopy was used to probe the physical state of neutral niobium species in the ablation plume at nine different process conditions. The goals of these measurements are threefold: first, to provide basic-level empirical data to be used in validating a computer simulation of the process; second, to identify hitherto unnoted phenomena within the plume which must be incorporated in improved modeling efforts; third and finally, to produce a means for monitoring process dependent variables (e.g. yield and particle size) by correlating observed features in the spectroscopy data with these process variables. Each of these goals has been achieved in some measure.

3.1. Laser Absorption Spectroscopy

A brief summary of the absorption spectroscopy diagnostic follows. A fuller description may be found in References [40-42] or in annual reports from previous years. The main advantage of the technique over other forms of spectroscopy rests in its optical simplicity—collection optics and expensive, fragile detectors are not necessary—and its ability to directly probe nonradiating low-lying atomic levels which are more populous, producing large signals even at relatively low temperatures. These two characteristics allow accurate and fairly simple determinations of densities.

In laser absorption spectroscopy, a narrowband, tunable-wavelength laser at low power is directed through a viewport in the processing chamber, through the region where the ablation plume exists. Upon exiting the chamber through another viewport, the transmitted laser beam impinges on a photodiode. By sampling the photodiode signal (gate time: 30 ns) immediately prior to and during the ablation process, it becomes possible to monitor the changes in transmitted power due to the presence of the ablation plume. If the laser wavelength is tuned to resonance with a spectral line of one of the atomic, ionic, or molecular species within the plume, the amount of laser power absorbed may be related to the population density of the quantum state that represents the lower level of the species' spectral transition. A spatially inhomogeneous absorbing medium, such as the ablation plume presents extra complications in data analysis, but from multiple measurements of the absorption in different region s of the plume, a full three-dimensional density distribution may be recovered. By probing different spectral lines, it is possible to measure the density distributions of several distinct quantum states.

Comparison of these permits the assignment of a temperature value for each spatial position, usually referred to as the excitation temperature. Once such a temperature distribution is obtained, population densities of all quantum states (of the species probed) may be inferred; these, in turn, may be summed to give a total density distribution within the plume for the species probed. Thus density and excitation temperature are measurable.

In addition, the probe laser beam may be set at different distances from the target; the delay between the initiation of the ablation plume (i.e. arrival of the processing excimer laser pulse at the target) and the onset of the absorption signal may be measured. This delay represents the time required for the leading edge of the ablation plume to travel so as to intersect the path of the probe laser beam. Dividing the distance between probe laser beam and the target by this delay time yields a propagation or expansion velocity of the plume in the axial direction.

Further data on atomic velocities may be extracted from a study of the variation of absorption with probe laser frequency within a single transition. This is referred to as the "absorption lineshape." The specific lineshape expected is very dependent on circumstances of temperature, but for the conditions expected to obtain within an ablation plume, the dominant physical process determining the lineshape is the Doppler effect. The Doppler effect causes atoms with differing velocity components along the direction of the probe laser beam to absorb most strongly at (slightly) different optical frequencies. A distribution of velocities thus results in a broadening of the range of wavelengths within which absorption on a specific atomic transition takes place, with the absorption strength at a particular optical frequency being proportional to the percentage of atoms possessing the velocity requisite for strong absorption on the frequency. Thus, the absorption lineshape can be associated with the distribution of velocity components along the probe laser propagation direction. In the case of thermal equilibrium, the expected velocity distribution produces a normal (gaussian) shape to the absorption curve. The width of the peak may be related to the temperature of the velocity distribution. Studying the absorption lineshape in ablation plumes can provide two important physical results: 1) a measure of the velocity distribution in directions transverse to the axial direction, and a consideration of to what degree this distribution represents a thermal distribution, and 2) if the distribution is thermal, a temperature measurement. Such a temperature is usually referred to as a kinetic temperature. Comparison of this to the excitation temperature can resolve questions about the interaction between different thermalization processes within the plume.

3.2. Experimental Apparatus

Figure 3.1 depicts the experimental apparatus. The probe laser is a Coherent 899-29 ring dye laser pumped by an argon ion laser. The dye and ring cavity optics are chosen to lase in a wavelength region of 410–420 nm. This represents a spectral domain where on plume species, neutral niobium, possesses a wealth of lines with characteristics suitable for the diagnostic used. The dye laser output beam is directed through a glass viewport in the process chamber through the region between the target and substrate. The beam propagates parallel to the target surface (for the orientation of Fig. 3.1, the target would emerge from the plane of the paper at an angle of 45°). Positioning of the beam within the plume is performed by translating a lens in directions parallel and orthogonal to the target surface; this lens also focuses the laser to a 100 µm diameter within the plume. The beam exits the chamber via a second glass viewport and is refocused to impinge upon a fast photodiode/amplifier detector (rise time ~100 ns). Sampling of the absorption signal exiting the detector is performed by a boxcar integrator whose output is fed to data acquisition inputs of the personal computer system that acts as a controller for the dye laser. A digital oscilloscope (not depicted) is employed to establish correct boxcar gate width and delay times and for time-of-flight measurements (axial expansion velocity). Absorption data is stored to hard disk, then transferred to a workstation for analysis.

3.3 Summary of Past Work

3.3.1. Year One

The first year of work on this project was devoted principally to 1) procurement of a vacuum/processing chamber, 2) design and construction of target and substrate holders, cooling block, etc., 3) test ablation runs on pure niobium targets, 4) modification of dye laser for use in the appropriate wavelength regime, and 5) identification of spectral lines appropriate for use as diagnostics. There were two primary challenges in these items, from the diagnostic standpoint. The first of these was to achieve a design for the target/substrate/chamber configuration satisfactory to both processing and diagnostic needs. The second was obtaining acceptable performance from the probe laser. The dye laser proper was specified to work in this wavelength region, but the dye laser *system* (i.e., computer controlled tuning and wavelength measurement) were not. Significant calibration efforts were required to obtain accurate wavelength measurements. By the

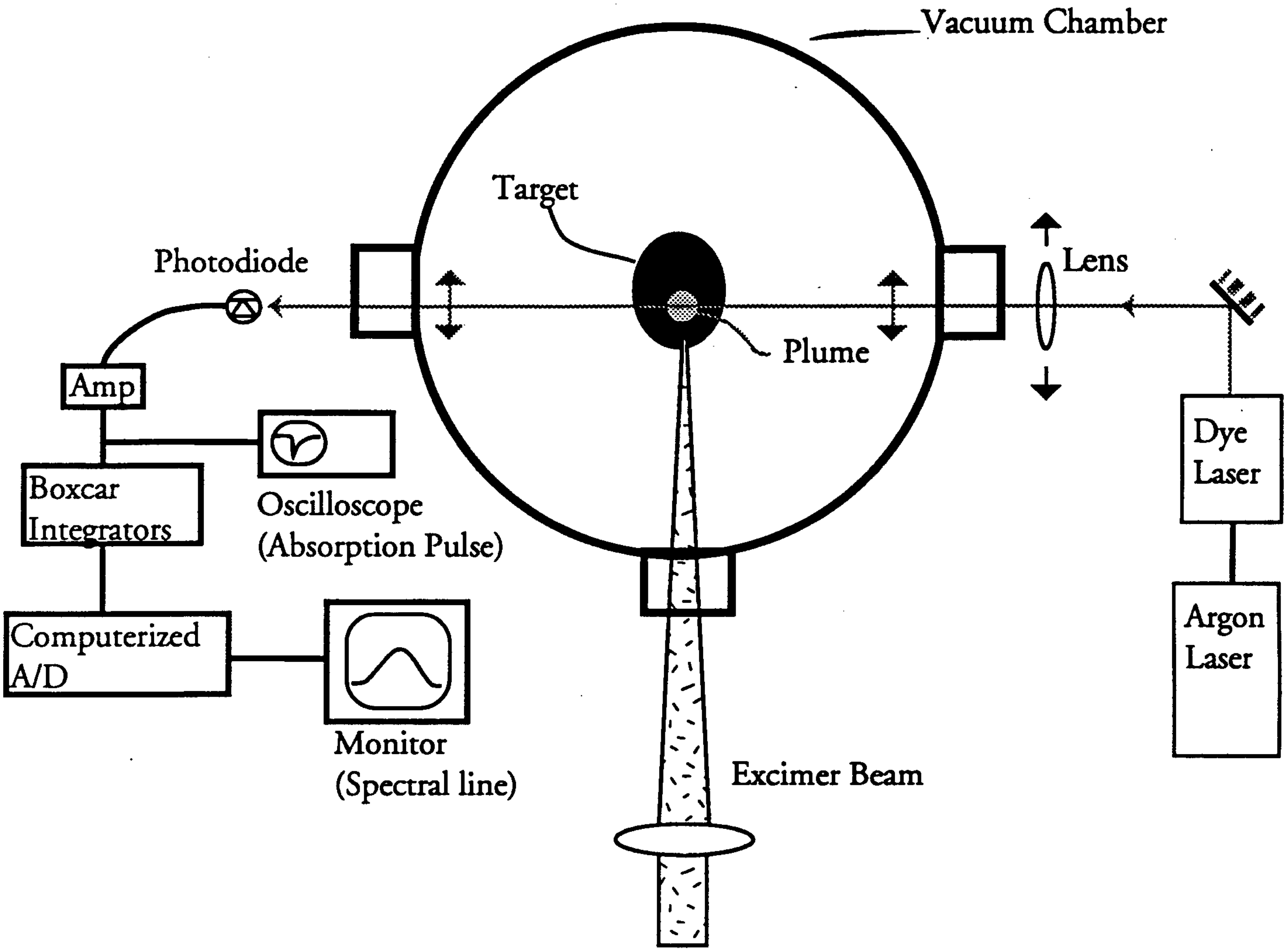

Figure 3.1. Experimental Apparatus for Absorption Spectroscopy.

end of the first year, absorption signals had been observed on a number of transitions for the neutral atomic species in ablation of pure niobium targets.

3.3.2 Year Two

In the second year, the gains of the first year were consolidated. Forty-three spectral lines of neutral niobium identified as being within the dye tuning range. Selection of five of these for use in the diagnostic measurements proceeded according to criteria of strength, energy levels involved, and nearness of other suitable lines. Details can be found in the relevant annual report[23] A matrix of independent process variables (three excimer laser powers and three ambient helium pressures) was selected. Three absorption transitions were probed for each set of process conditions. Initially, it was intended that absorption data for the different process conditions be taken at the same gate delay, i.e. the same time after the arrival of the excimer pulse. The variation in expansion velocities between different pressures prevented this. Therefore, data for gas pressures of 1.0 and 10 Torr were taken at a delay time of 1.6 μs, while a 0.66 μs delay was used for the 0.1 Torr runs, and a single 1.0 Torr run. A data analysis program for extracting density and excitation temperature was written. Total densities were calculated on the basis described above.

Figures 3.2–3.4 show (total) density profiles for the process conditions. In data analysis, the ablation plumes are assumed to possess axial symmetry. In the figures, the vertical axis represents the symmetry axis, i.e. the distribution is a solid of rotation about the vertical axis with the target surface located on the horizontal axis (y=0). Note that the peak density values (i.e., the range of the color bar representing the z-axis) are significantly lower than values given in previous annual reports. This is due to an error in earlier data analysis. The *relative* densities, i.e. the shape and dimensions of the plume are unchanged from the earlier reports. The most apparent feature in these graphs is the variation in evolution speed of the plume under different process conditions. This is particularly true for different helium pressures—the lower the pressure, the quicker the evolution/expansion. It should be noted once more that the 0.1 Torr data (Fig. 3.2). This accounts for the apparently smaller size of these plumes. In actuality, had the 0.1 Torr data been collected at the longer delay time, no absorption signal would have been observed, since the plume propagated beyond the viewport's visual access. The 1.0 Torr plumes appear to have their leading edges just beyond the observation region.

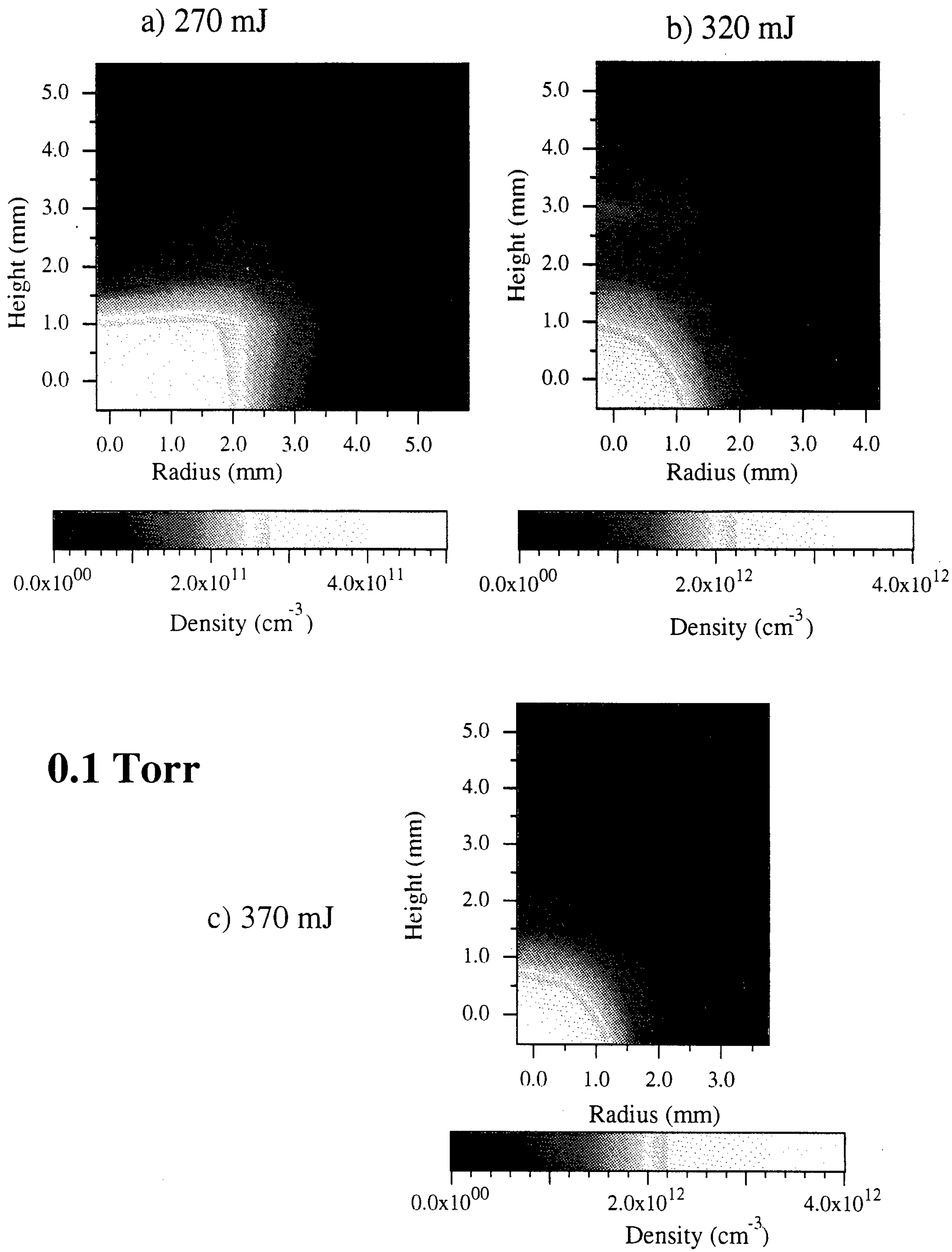

Figure 3.2. Total Density Distributions for 0.1 Torr Process Conditions

a) 320 mJ

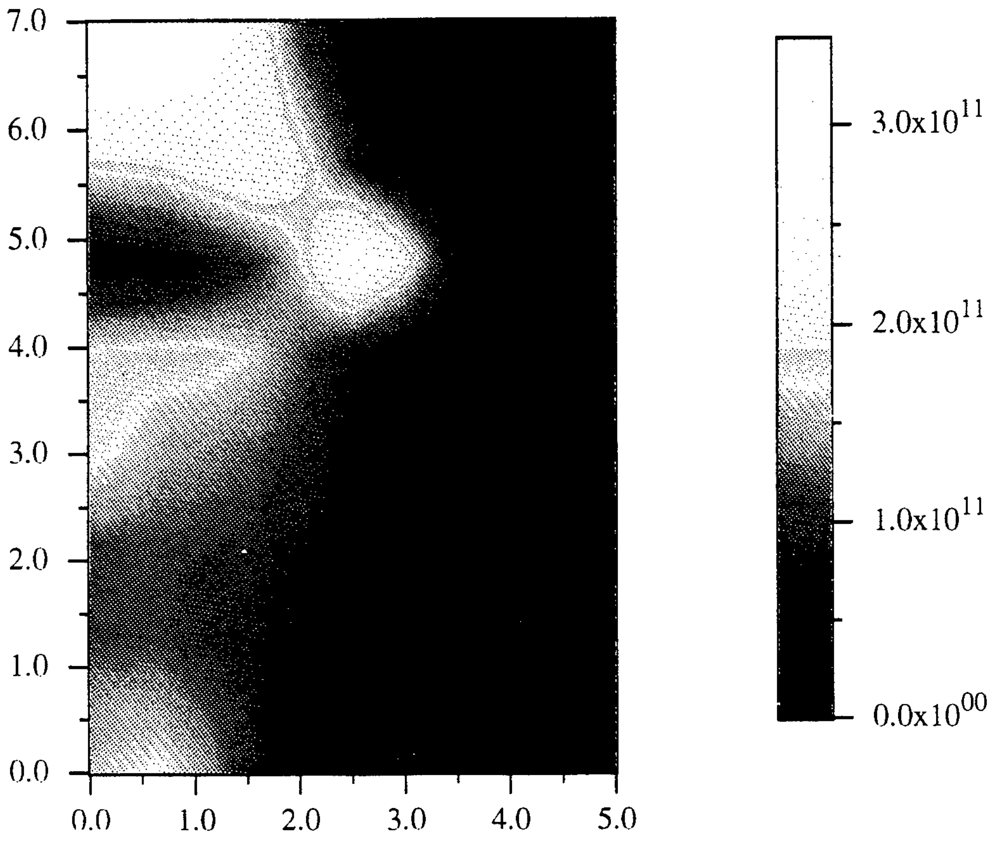

b) 370 mJ

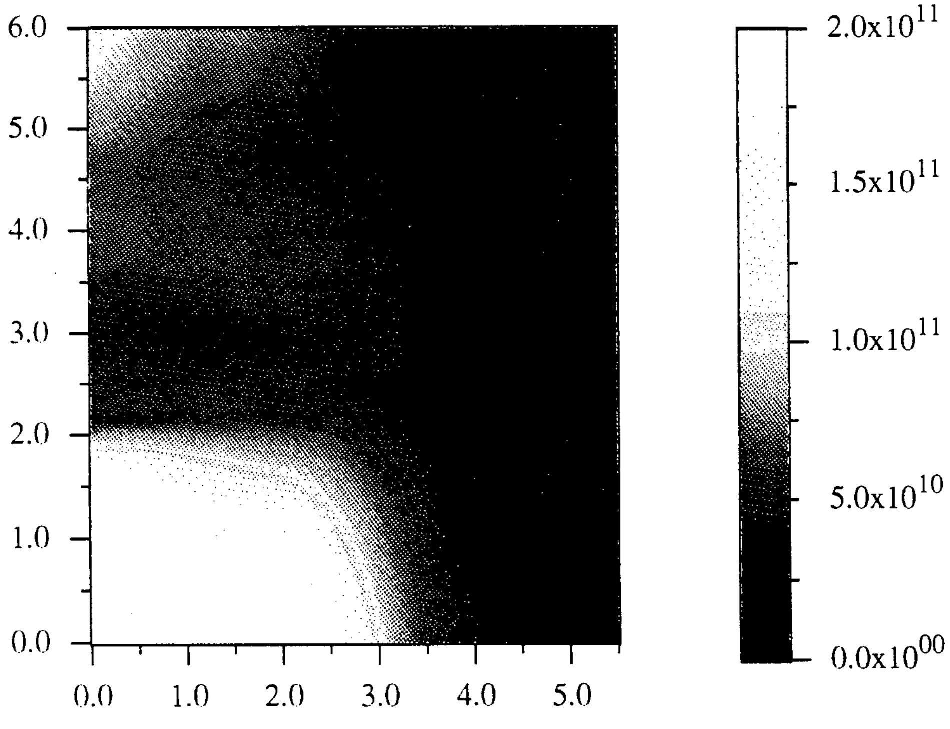

Figure 3.3. Total Density Distributions for 1.0 Torr Process Conditions

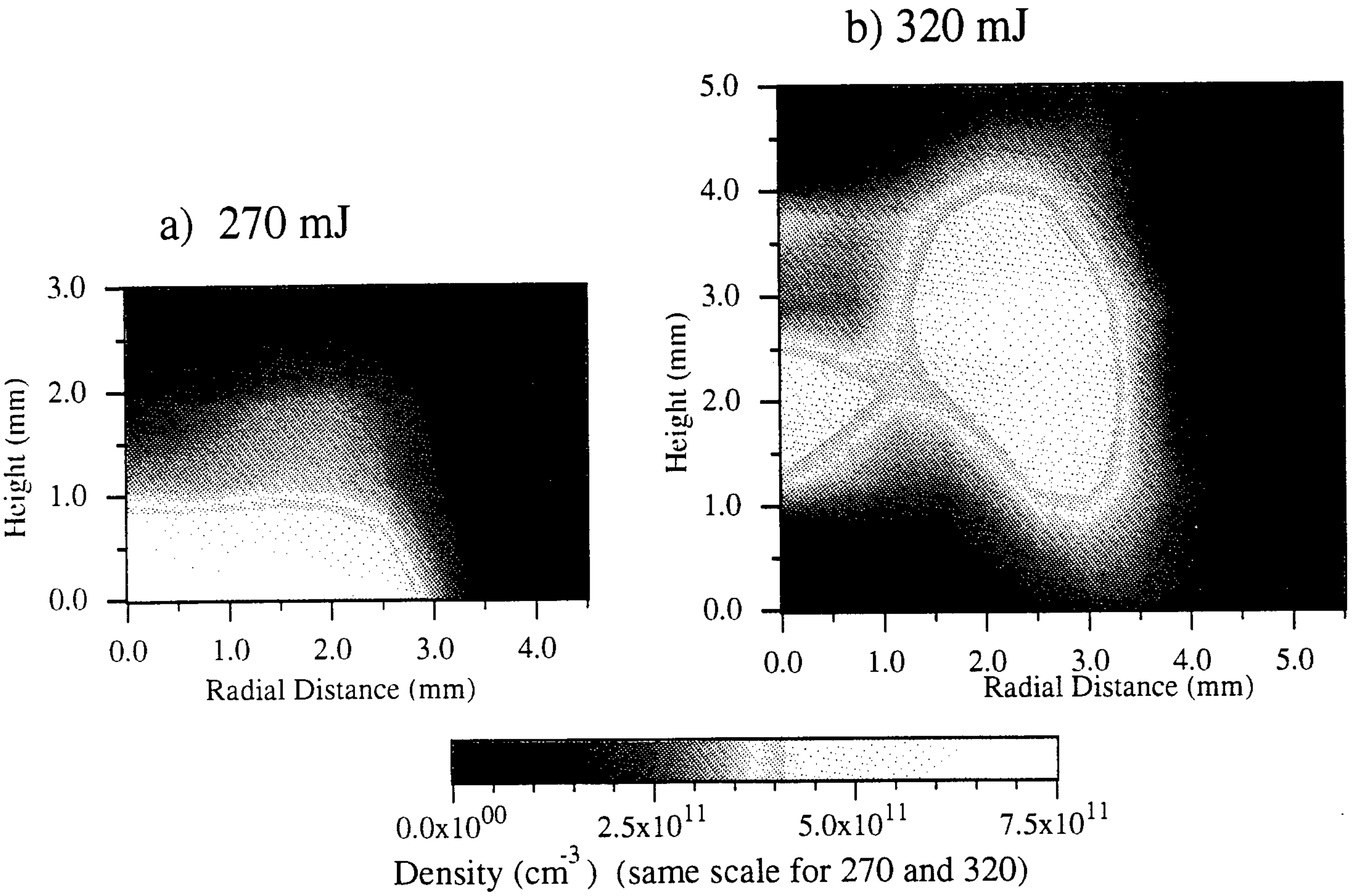

c) 370 mJ

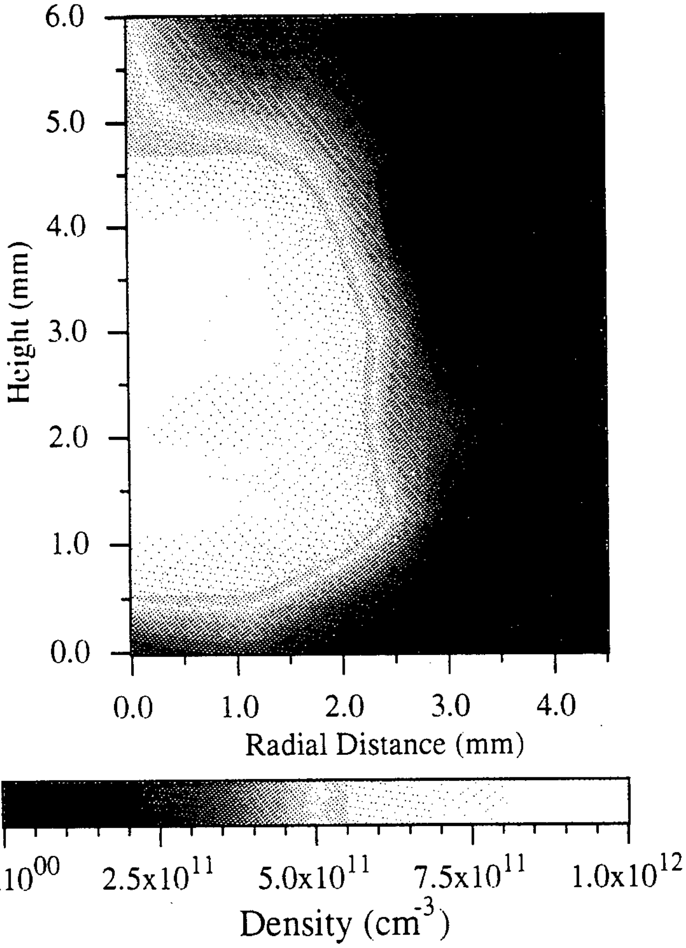

Figure 3.3. Total Density Distributions for 10 Torr Process Conditions

Figures 3.5–3.7 provide the complete set of measured excitation temperature distributions. A representative sample set of these graphs were a part of a previous report.[23] The most noteworthy feature of these graphs is the uniformity of temperature throughout the plume, typically temperatures vary by no more than 10–20% over spatial regions where density varies by orders of magnitude. Generally, an increase in excitation temperature with height above the target surface was observed; this suggests that the faster moving atoms at the leading edge either leave the surface in higher excited states, or more efficiently convert their excess kinetic energy into internal energy through collisions with the background gas. The near-uniformity of excitation temperature suggests that the expansion is very nearly isothermal for the pressures considered. This might be alternatively stated as saying that the plume expansion proceeds much faster than the mechanisms for thermal redistribution in the plume, essentially "freezing in" a particular excitation temperature. This claim could be verified by tracking the temperature distributions at multiple delay times, i.e. many different times during the plume evolution. Note that the increased collisional interactions expected at higher background gas pressures should both slow the plume expansion in speed up the thermal redistribution process, resulting in increased differences in temperature across the plume. This corresponds with observations.

Excitation temperatures are necessary for calculating the total density of niobium atoms from the spectroscopic measurement of population density of a single level. Thus the data shown in Figs. 3.2–4 rely upon the data in Figs. 3.5–3.7. It is the *total* densities that are of most interest, since they are expected to reflect the ablation rate from the target. Spatial integration of the total density distributions gives values for the total number of free neutral niobium atoms within the plume, which should correlate to the total number of Nb atoms removed from the target by an excimer pulse. Spatial integrations of the density distributions of Figs. 3.2–3.4 were performed. These data will be presented in a later section of this chapter(*Year Three)*, where they are compared to process data on the ablation rate. It was notable that the results from the plume integrations suggested that the ablation rate does not increase significantly for increase of excimer pulse energy 320 to 370 mJ, suggesting that optimization of the ablation rate could not be achieved by moving to higher fluences (energy/unit area), but rather by increasing pulse energy *and* area to maintain constant fluence, while increasing the energy coupled to the target.

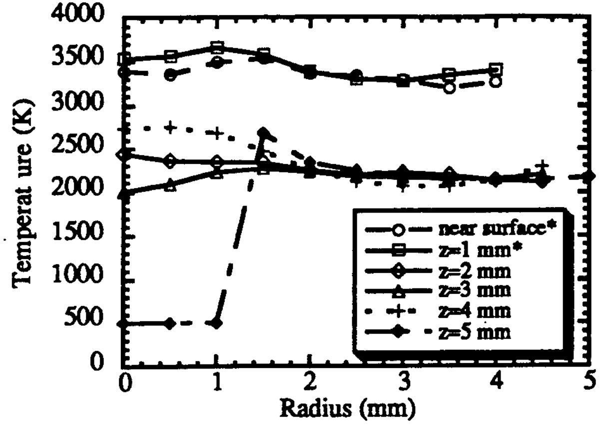

270 mJ Excimer Energy

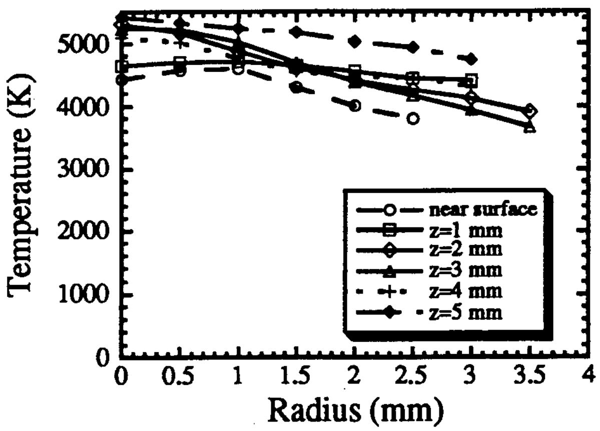

320 mJ Excimer Laser Energy

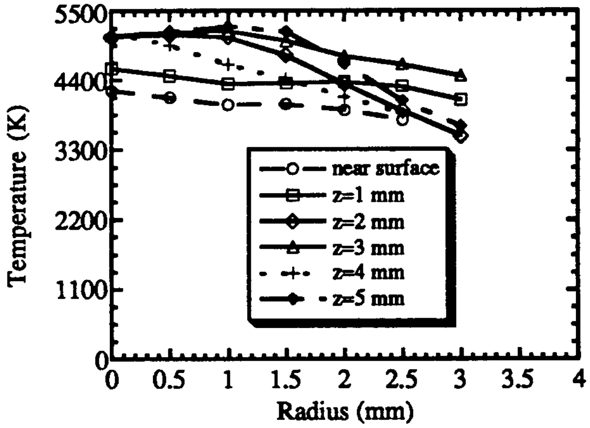

370 mJ Excimer Laser Energy

Figure 3.5. Excitation Temperature Distributions for 0.1 Torr Process Conditions.

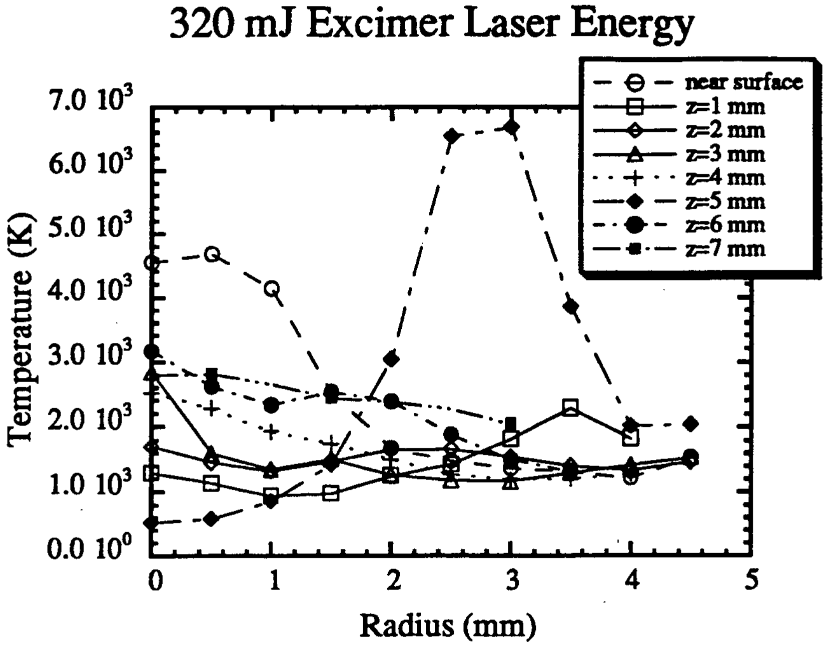

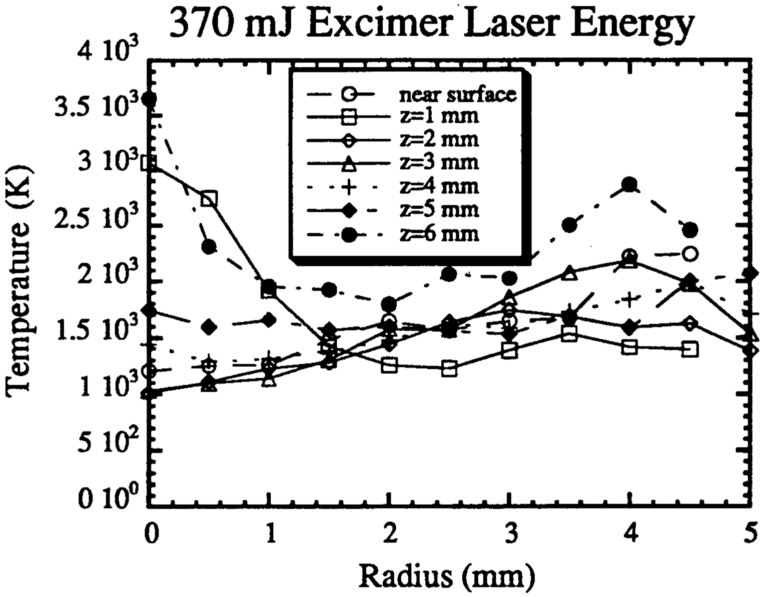

Figure 3.6. Excitation Temperature Distributions for 1.0 Torr Process Conditions.

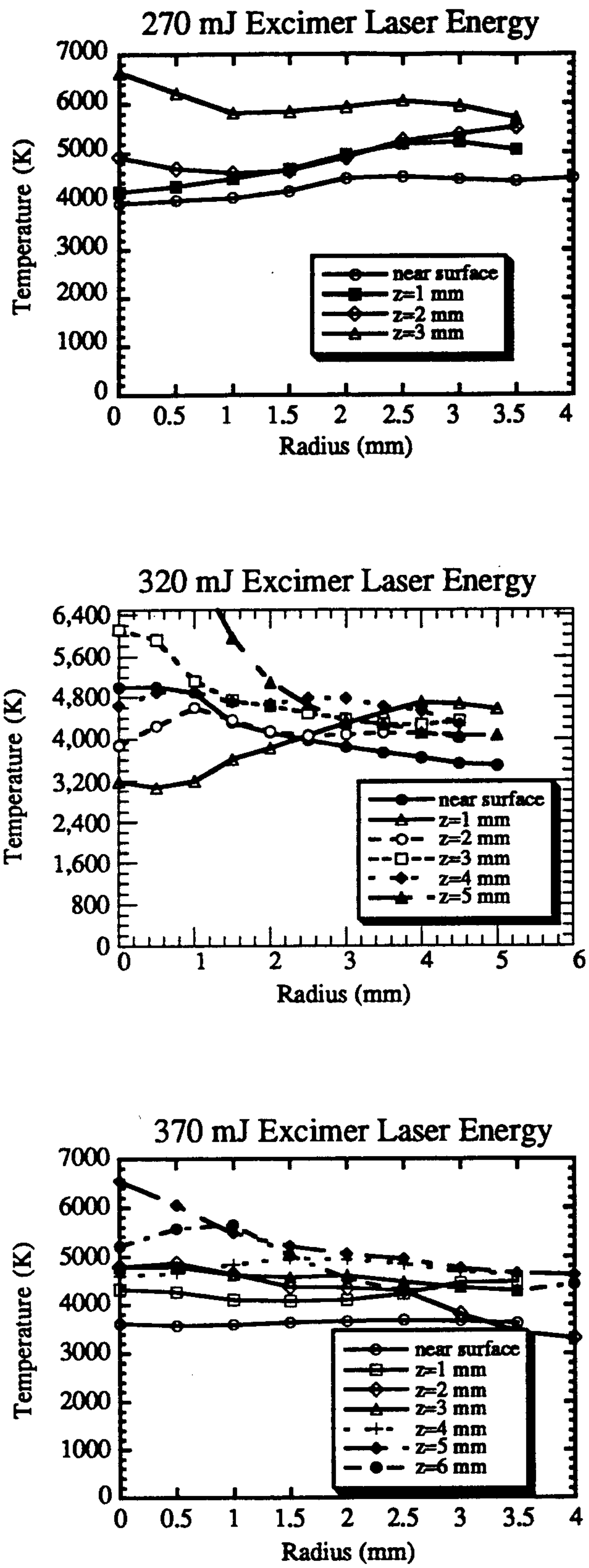

Figure 3.7. Excitation Temperature Distributions for 10.0 Torr Process Conditions.

The exact relation between the integrated-plume densities and the actual ablation rate depends upon the following factors: 1) the fraction of Nb atoms ablated from the target that leave as *free* atoms (as opposed to molecules/clusters), and 2) the fraction of ablated free atoms that remain free over the time delay between the excimer pulse and the absorption measurement and 3) the degree to which the ablation is stoichiometrically congruent. Comparison of the integrated-plume densities with independent measurements of ablation rate and stoichiometry of deposited powder accomplishes a dual purpose—calibration of the spectroscopic technique and insight into the processes that determine the above-cited factors. Thus, further interpretation of these results is dependent on post-process characterization measurements. A more extensive discussion of this topic is deferred to the preceding section of this report *(Year Three).*

3.4. Results in Past Year

The optical diagnostics work in the final year of this project falls into three main categories: 1) Time-of-flight measurements of plume expansion, 2) Kinetic temperature measurements from absorption lineshape and 3) Comparison and correlation of spectroscopy results to process data and numerical model.

3.4.1 Expansion Speeds

He Pressure (Torr)	Excimer Pulse Energy (mJ)	Max. Axial Velocity (× 10^5 cm/s)	Max. Radial Velocity (× 10^5cm/s)
0.1	270	4.5	5.3
	320	7.5	3.8
	370	6.1	3.6
1.0	270	n/a	n/a
	320	4.7	1.3
	370	5	2.8
10.0	270	1.5	2.3
	320	3.9	2.5
	370	4.1	2.1

Table 3.1. Plume expansion velocities.

Time-of-flight measurements of plume expansion are summarized in Table 3.1. As expected, the expansion slows with increasing gas pressure. Also note that axial velocity generally increases with laser pulse energy, with a dramatic increase from 270 mJ to 320 mJ and a lesser increase (actually, a slight decrease for 0.1 Torr data) from 320 mJ to 370 mJ. This behavior is similar to the changes in integrated plume density, and is consistent with the interpretation that excess pulse energy goes into kinetic energy of the plume, rather than ablating more material . The plume expansion speeds in the radial direction exhibit no clear pattern of variations with pulse energy.

3.4.2 Kinetic Temperatures

The uniformity of excitation temperatures suggests that the kinetic temperatures may not exhibit large variations with position within the plume. This implies that the absorption lineshapes may be simple Gaussian peaks with an easily-interpreted (kinetic) temperature. Figures 3.8–3.10 show sample absorption curves (data points) and the best-fit Gaussian (solid lines) as obtained using χ^2-minimization via a Levenberg-Marquardt algorithm. The fit to the Gaussian lineshape is excellent. By redirecting the probe laser beam through different parts of the plume, some confirmation of uniformity was possible. Observed differences in linewidth (FWHM) were typically no more than 10–15% for comparison between laser directly through center of the plume and just clipping the periphery. Even these differences may be accounted for by degradation in signal at the periphery where the atomic density is low. A "plume-avaeraged" value for linewidth was calculated for each process condition, along with associated temperature, mean velocity and mean atomic kinetic energy. These values are summarized in Table 3.2.

Helium Pressure (Torr)	Excimer Pulse Energy (mJ)	Doppler Linewidth (GHz)	Temp. (K)	<v> (×10^5 cm/sec)	Mean K.E. (eV)
0.1	270	18.0	310,000	8.4	51
	320	19.8	376,000	9.2	61
	370	19.5	365,000	9.1	59
1.0	270	12.6	260,000	6.5	42
	320	12.3	257,000	6.4	41.5
	370	11.9	253,000	6.3	41
10.0	270	10.2	100,000	4.8	23
	320	8.4	64,000	3.9	15
	370	8.5	65,000	4.0	16

Table 3.2. Doppler Linewidths and Kinetic Temperatures Summary.

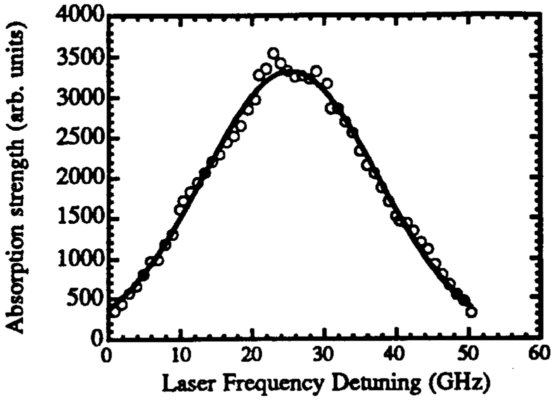

Figure 3.8. Sample absorption peak and gaussian fit for 0.1 Torr He, 370 mJ/excimer pulse.

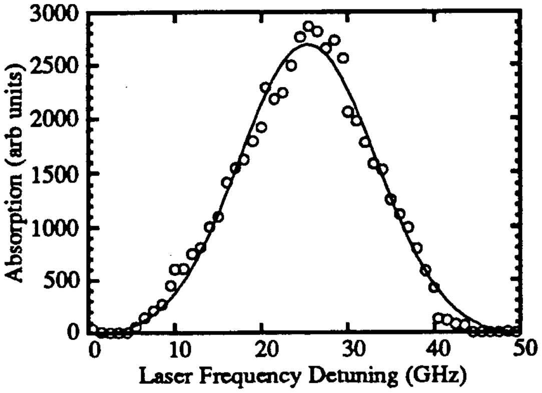

Figure 3.9. Sample absorption peak and gaussian fit for 1.0 Torr He, 370 mJ/excimer pulse.

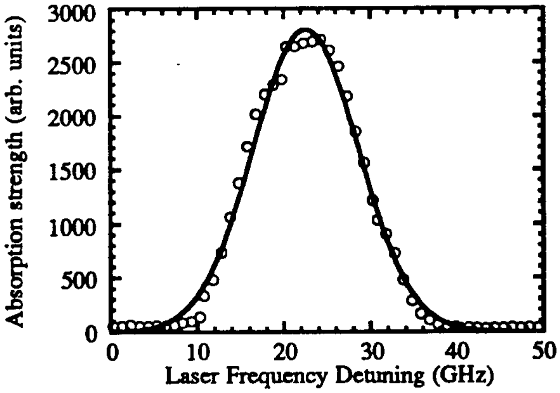

Figure 3.10. Sample absorption peak and gaussian fit for 10 Torr He, 320 mJ/excimer pulse.

Considering Table 3.2, the most striking feature is the high kinetic temperature values. These exceed the excitation temperature by one to two orders of magnitude. It should be noted that the mean velocities and kinetic energies associated with such temperatures are not particularly surprising—others researchers have recorded similar values using different methods, and in fact the mean velocities are of the same order as the expansion front speeds discussed in the time-of-flight measurements What is surprising is that the velocity distribution is thermal (i.e., gaussian lineshape), indicating a strong thermalization process to redistribute velocities. The population distribution amongst internal (atomic) states can likewise be demonstrated to obey the proper thermal distribution (i.e., Boltzmann),[41] but the temperatures from these two measurements are widely at variance. This appears to suggest that there are well defined thermalization mechanisms acting for each kind of temperature, but little coupling between the two mechanisms. Excitation of atomic levels is usually assumed to be dominated by inelastic collisions of neutral atomswith free electrons in the medium, due to the much stronger electromagnetic interaction associated with one collisonal partner being charged. This is the mechanism which determines the excitation temperature. Elastic collisions between partners of near-equal mass (i.e., two neutral atoms or atom-ion) are far more efficient at transferring kinetic energy than elastic collisions between unequal mass partners (free electron-atom), because of the need to conserve of both energy and momentum in elastic collisions. Thus, collisions between atoms is the determinant of the kinetic temperature. The difference in temperatures suggests that the free electron kinetic temperature is much lower than the atomic kinetic temperature. This could occur if the free electrons distribution is created at low temperatures/kinetic energies relative to the massive components. This could be studied by observing the population distribution and linewidths for earlier times in the plume evolution. This appears to be a promising area for future work.

Another aspect of the linewidth data is that the *mean* atomic speeds from these measurements are comparable or exceed to the *maximum* speed of the plume expansion front. This implies that the expansion is essentially diffusive, even for low pressures. Computer modeling of this process, to date, has only been performed assuming free expansion into vacuum. Correct incorporation of background gas effects into the model will rely on these data.

Finally, it is notable that the kinetic temperatures decrease with gas pressure, while the excitation temperatures increase, suggesting that the higher collisional frequency associated with higher gas pressure works to pull the two temperature distributions into equilibrium. However, the increase in internal energy fails to balance the loss of kinetic energy. The remaining energy is no doubt transferred to the background helium.

3.4.3. Relation of Diagnostic Data to Other Areas

The spectroscopic experiments were intended to function as model validation tests and process monitors. Consideration of the spatially-integrated density distributions in relation to an independent ablation rate measurement fulfills both these aims. The $NbAl_3$ target was weighed before and after each process run, and the number of pulses striking the target for each run was recorded. Thus, an independent calculation of ablated mass per pulse is possible, assuming the material removal did not vary from the beginning to the end of a process run. Comparison of these values to values obtained from the spectroscopic measurements are shown in Figs. 3.11–3.13. Each graph shows these ablation rates as a function of pulse energy for a particular gas pressure. Comparison between different gas pressures is less meaningful due to the differences in gas interaction and delay times at which the data were collected. The vertical axis for the spectroscopy-derived values includes mass of ablated aluminum by assuming the ablation is stoichiometrically congruent to the deposited powders (this data from the Processing chapter). The graphs show a clear correspondence between the actual ablation rate and the values inferred from absorption spectroscopy. Thus, by monitoring the absorption signal strength, changes in the ablation rate (due, for example, to decreased transmission of the chamber window, or dirty optics) could be detected and corrected. Note that changes in gas pressure are less likely to be detectable by this means, since the plume propagation speed and temperature changes dramatically with gas pressure. In any case, there are more economically viable methods for monitoring the ambient pressure.

The spectroscopic data on total Nb mass within the plume also provides important validation of the computer model.[43] The model predicts that significant nucleation takes place over the duration of the excimer pulse (30 ns), implying that by delay times long compared to the excimer pulse length (such as the 1.6 and 0.66 μs delays used for the spectroscopy measurements) a very small fraction of the material in the plume will exist as free atoms. Comparing the y-axes for the pairs of curves in Figs. 3.11–3.13, we see scaling factors in the range 30–200 for the different process conditions, confirming that most of the Nb is in forms invisible to the absorption technique, e.g. molecules or ions. The latter of these is extremely unlikely given the measured excitation temperatures, and in fact, an attempt to observe absorption o the sole ion transition

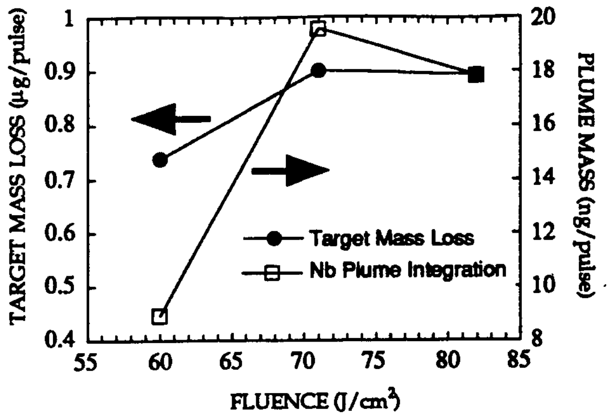

Figure 3.11. Comparsion of ablation rates: 0.1 Torr data.

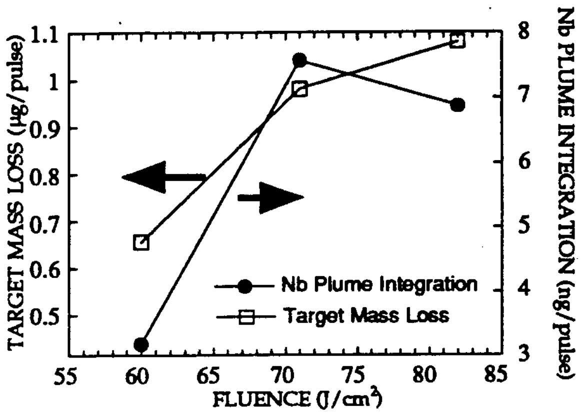

Figure 3.12. Comparison of ablation rates: 1.0 Torr data.

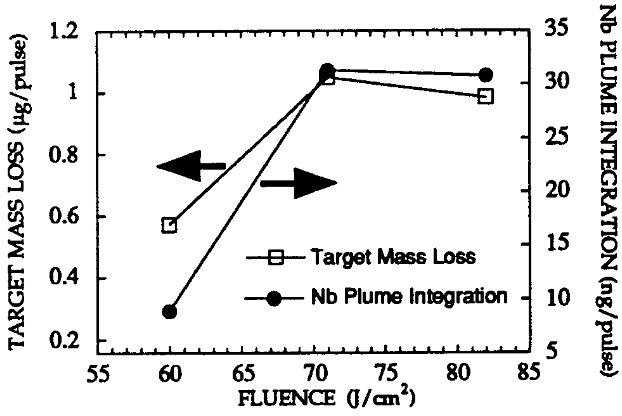

Figure 3.13. Comparison of ablation rates: 10.0 Torr data.

within the tuning range of the dye laser produced zero signal. Thus the conclusion that up to 99.5% of the material is in the form of molecules and clusters is reasonable and supports the model.

More broadly, the density and temperature data obtained via the spectroscopy diagnostic will form important guidelines for improving the gasdynamic aspect of the model. At present, the specification of the velocity and excitation distributions of atoms leaving the surface is of necessity oversimplified. Calculating these distributions from first principles would be prohibitively difficult. With the detailed characterizations available from the diagnostic data, it becomes possible to incorporate these factors into the model phenomenologically, the empirical data providing boundary conditions for the expansion dynamics.

Another potential process monitoring application arises from a detailed consideration of the ablation rate and particle size data. The ablation rate is observed to roll off at higher powers, while particle size is observed to decrease under the same conditions. Conservation of energy requires the increase in laser energy be transferred into some degree(s) of freedom of the already-ablated material, since it is not consumed in freeing a greater mass from the target. It seems reasonable to conclude from the particle size data that the laser energy is transferred into higher initial kinetic energy of the plume mass, which can be expected to frustrate nucleation in the plume. That is, the greater kinetic energies of plume constituents requires more elastic collisions to shed sufficient kinetic energy for bonding to take place. For fixed ambient pressure, the mean free path, and thus the number of collisions, is fixed, so higher initial plume kinetic energies lead to smaller particles. Thus we would expect that a measure of kinetic energy would provide insight into the mean particle size. The most meaningful way to measure this factor is via the axial expansion velocity, since this represents the plume constituents that eventually come to be deposited on the substrate. Constituents with large radial velocities (which would be measured by the Doppler linewidth of the absorption curve) will tend to miss the substrate.

Figure 3.14 depicts a simultaneous graph of particle size and axial velocity vs. ablation pulse energy for the 10 Torr data. The expected inverse relation between velocity and particle size is evident. Thus monitoring the delay time between the excimer pulse and onset of the absorption signal could be used for fine control of gas pressure and laser power to maintain constant particle size.

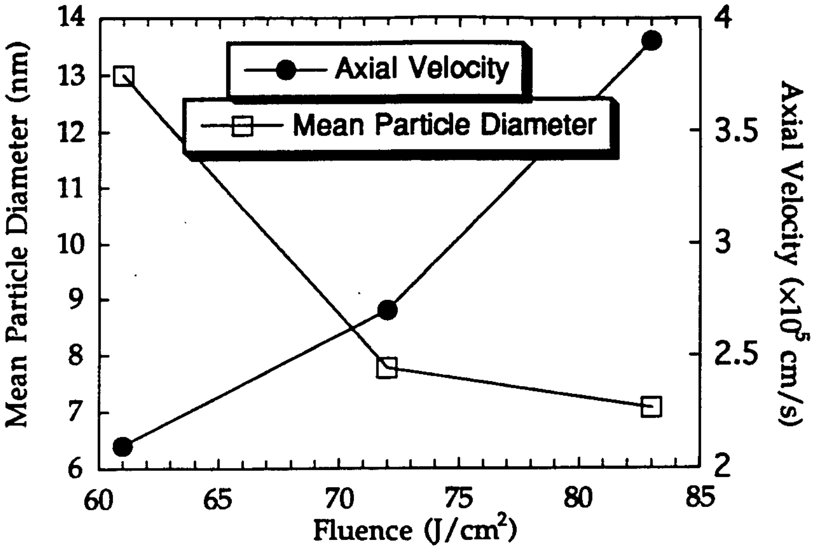

Figure 3.14. Inverse relation between particle size and axial velocity for the 10.0 Torr process runs.

3.5. Summary

Laser absorption spectroscopy has proved to be an important and flexible tool for diagnosing laser ablation plumes. Its greatest value as a tool for understanding the basic physics of the process rests in its ability to measure absolute density distributions of majority-population low-lying energy states of plume species, thus permitting establishment of what fraction of the plume mass is observed. The technique also permits measurements of plume temperatures and expansion speeds. We have used this technique to uncover new aspects of behavior in the ablation plume, thereby improving and validating computer models of the process. Further, we have demonstrated correlations between observed diagnostic trends and dependent process variables, thus creating rudimentary process monitors. Full-scale employment of this technique must wait upon two developments: 1) more detailed (empirical) characterization of the relation between the process variables and the diagnostic signals, and 2) development of low-cost, compact, rugged tunable laser sources in the appropriate wavelength regions (e.g., near-UV and violet/blue). Recent developments in diode laser research and fiber lasers [44]suggest that this last obstacle may be surmounted within 5–10 years.

Chapter 4. Computer Modeling

Nanosize particles have several interesting features for synthesizing new materials with improved properties as compared to the coarser-grained conventional materials, but the rate of production of such particles in various processes is usually very low. However, laser ablation is expected to give a higher yield. In this chapter, a gas-dynamical model[43] is discussed for analyzing the plasma formation and the velocity and particle-size distribution in the plasma during laser ablation. The melting and evaporation rates are determined by using the heat conduction equation and the Stefan condition. To account for the discontinuity of various state variables across the Knudsen layer, jump conditions are used; the gas-dynamics equations are solved to study the convective flow of the metal particles in the region above the Knudsen layer. Plasma physics is used to model the formation of plasma and to compute the laser-beam attenuation coefficient and ion concentration within the plasma. The particle-size distribution in the plasma is determined by using a droplet-growth theory.

Main results of the model include:

1) More material melts and vaporizes as the laser intensity of the ablation time increases. Only a very small amount of material vaporized during a single pulse, but the vapor flux generated is large.

2) The temperature and vapor flux at the vaporization front increase rapidly during the first several nanoseconds of the pulse, then become constant near the end of the pulse.

3) The radial and axial velocities vary from a few to several hundred meters per second.

4) The plasma formed during the pulse is very weakly ionized; the ion mass fraction increases as one moves toward the plasma boundary, or as residence time of the ablated material in the plasma increases.

5) Nanoscale particles exist near the vaporization front. The particle size increases as one moves toward the plasma boundary or as residence time within the plasma increases.

6) Energy losses due to conduction in the target, absorption and scattering due to the plasma and vapor phases, conversion of thermal energy into kinetic energy of the ablated products, and losses from the target surface due to conduction, convection and radiation are important factors in correctly predicting the empirical ablation rates.

7) The trend between theoretical and experimental results[13] is similar, but the theoretical predictions are higher than the experimental values, possibly due to the multiple paths for energy loss and the lack of reliable high-temperature data for the thermal constants of the material.

Chapter 5. Laser Cladding Experiments

The laser cladding process is being extensively used for synthesis of coatings and for repair of aerospace jet engine components with high performance alloys for specialized applications. Although the mechanism of laser cladding, and the effects of various process parameters on properties of the clad have been studied in detail, the research in the area of real-time diagnostics and process control has been lacking. $NbAl_3$, an extremely brittle intermetallic line compound is a prime candidate for high temperature structural applications because of its low density, high melting point, and the best oxidation properties among all the Nb-Al alloys. Growth of a protective α-Al_2O_3 layer on $NbAl_3$ during isothermal oxidation in air is not sustained, however, due to formation of an Nb_2Al layer beneath the oxide layer which oxidizes into $NbAlO_4$. At temperatures between 650 °C and 800 °C, $NbAl_3$ disintegrates, due to rapid grain boundary oxidation known as the 'pest phenomenon'. Attempts to improve the ductility of $NbAl_3$ by transforming crystal structures from DO_{22} into Ll_2 by macroalloying have not been successful. Macroalloying of $NbAl_3$ has led to the development of oxidation resistant, but brittle, alloys.

Spectroscopic diagnostics based on plasma optical emission spectroscopy have been employed in this investigation to infer composition, thickness, and temperature of the clad during laser cladding of Nb-Al-Hf alloys on Nb substrates. The results indicate that both continuum and characteristic line emission may be used to monitor variations in thickness of the clad and laser power used for cladding, although line intensities are much more sensitive. Clad temperature, inferred from the calculated plasma temperature, is found to be inversely proportional to the thickness of the clad. The intensities of Nb-I and Hf-I characteristic emission lines are directly, whereas the Al-II line is inversely, proportional to the thickness of the clad. The Nb-I to Al-II line intensity ratio and continuum intensities are directly proportional to laser power and to the thickness of the clad. Nb-I to Al-II and Nb-I to Hf-I intensity ratios increase, and Al-II to Hf-I decreases, linearly with increase in concentration of Nb within the clad. The correlation between the Nb-I/Al-II intensity ratio and concentration of Nb depends on the physical and chemical states of the alloying elements present in the initial powder mixture, as well as the microstructure and constitution of the phases forming the clad. Therefore, local variation in the composition of the clads may be monitored by measuring the intensity of characteristic emission lines.

Isothermal oxidation behavior of laser clad $NbAl_3$-based alloys with addition of up to 1.0 at. % B, 1.5 at. % Hf, and 3 or 6 at. % Ti has been evaluated at 800 °C, 1200 °C, and 1400 °C. None of the alloying additions improves the ductility of $NbAl_3$ or produces a crystal transformation from DO_{22} to the more ductile Ll_2 structure. Alloys containing Al-rich interdendritic phases exhibit the best oxidation resistance and form, at all three test conditions, an outer layer exclusively of α-Al_2O_3 by outward diffusion of Al, irrespective of the alloying additions, and no Nb-rich layer precipitates below the oxide layer. Presence of Al-rich phase and/or addition of Ti suppresses the occurrence of the 'pest phenomenon' at 800 °C. The oxidation resistance degrades as the fraction of Nb-rich phases (containing <75 at. % Al) in the alloys increases and a mixture of α-Al_2O_3 and $NbAlO_4$ forms upon oxidation. A Nb-rich layer also precipitates below the oxide layer in these alloys. Alternating layers of α-Al_2O_3 and $NbAlO_4$ form, however, at 1200 °C and 1400 °C only in $NbAl_3$ + 3 at. % Ti alloy containing Nb-rich probably due to increase in the diffusivity of oxygen. Addition of 1.5 at. % Hf to $NbAl_3$ improves its cyclic oxidation resistance at 1200 °C in air.

References

1. Birringer, R., H. Gleiter, H.P. Klein, and P. Marquarrdt: Phys. Lett., Vol. 102A, 1984, pp. 365.
2. Birringer, R. and H. Gleiter: ed. *Encyclopedia of Materials Science and Engineering,* ed. R.W. Cahn. Vol. Suppl. 1, Pergamon: Oxford, 1988, pp. 339.
3. Siegel, R.W., S. Ramasamy, H. Hahn, Li Zongquan, and Lu Ting: J. Mater. Res., Vol. 3, 1988, pp. 1367.
4. Lu, K., J.T. Wang, and W.D. Wei: J. Phys. D, Vol. 25, 1992, pp. 808.
5. Suryanarayana, C. and F.H. Froes: Met. Trans. A, Vol. 23A, 1992, pp. 1071.
6. Granquist, C.G. and R.A. Buhrman: J. Appl. Phys., Vol. 47, 1976, pp. 2200.
7. Eckert, J., J.C. Holzer, C.E. Krill III, and W. L. Johnson: J. Appl. Phys., Vol. 73, 1993, pp. 2794.
8. Flint, J. H. and J.S. Haggerty: Ceramic Transactions, Ceramic Powder Science II, Vol. 1A, 1988, pp. 244.
9. Hahn, H. and R.S. Averback: J. Appl. Phys., Vol. 67, 1990, pp. 1113.
10. Inoue, A., B.G. Kim, K. Nosaki, T. Yamaguchi, and R. Masumoto: J. Appl. Phys., Vol. 71, 1992, pp. 4025.
11. Iwama, S., K. Hayakawa, and T. Arizumi: J. Cryst. Growth, Vol. 56, 1982, pp. 265.
12. Chow, G.-M., P.G. Klemens, and P.R. Strutt: J. Appl. Phys., Vol. 66, 1989, pp. 3304.
13. Stafast, H. and M. von Przychowski: Appl. Surf. Sci., Vol. 36, 1989, pp. 150.
14. Powers, D.E., S.G. Hansen, M.E. Geusic, A.C. Pulu, J.B. Hopkins, T.G. Dietz, M.A. Duncan, P.R.R. Langridge-Smith, and R.E. Smalley: J. Phys. Chem., Vol. 86, 1982, pp. 2556.
15. Lundin, C.E. and A.S. Yamamoto: Trans. Metall. Soc. AIME, Vol. 236, 1966, pp. 863.
16. Shechtman, D. and L.A. Jacobson: Metall. Trans. A, Vol. 6A, 1975, pp. 1325.
17. Aindow, M., J. Shyue, T.A. Gaspar, and J.L. Fraser: Phil. Mag. Lett., Vol. 64, 1991, pp. 59.

18. Schneibel, J.H., P.F. Becher, and J.A. Horton: J. Mater. Res., Vol. 3, 1988, pp. 1272.

19. Haasch, R.T., S.K. Tewari, S. Sircar, C.M. Loxton, and J. Mazumder: Metall. Trans. A, Vol. 23A, 1992, pp. 2631.

20. Raisson, G. and A. Vignes: Rev. Physiq. Aplliq., Vol. 5, 1970, pp. 535.

21. Kawanishi, S., K. Isonishi, and K. Okazaki: Mat. Trans., JIM, Vol. 34, 1993, pp. 1993.

22. Yamamoto, T. and J. Mazumder: Nanostructured Mater., Vol. 1995, pp.

23. Mazumder, J., A. Kar, T.P. Duffey, and T. Yamamoto: *Synthesis of Nanocrystalline Nb-Aluminides by Laser Ablation Technique*, 2, Air Force Office of Scientific Research, 1994.

24. Cliff, G. and G.W. Lorimer: J. Microscopy, Vol. 103, 1974, pp. 203.

25. Miyamoto, I., T. Ooie, Y. Hirota, and H. Maruo: in International Conference on Applications of Lasers and Electro-Optics (ICALEO'93). Orlando: Laser Institute of America, P. Denney, I. Miyamoto, and B.L. Mordike, 1993, pp. 1.

26. Lothe, J. and G.M. Pound: J. Chem. Phys., Vol. 36, 1962, pp. 2080.

27. Allmen, M.F. von: *Laser Beam Interactions with Materials.*, Berlin: Springer, 1987.

28. Dam, B., J. Rector, M.F. Chang, S. Kars, D.G. DeGroot, and R. Griessen: Appl. Phys. Lett., Vol. 65, 1994, pp. 1581.

29. Ingen, R.P. van, R.H.J. Fastenau, and E.J. Mittemeijer: J. Appl. Phys., Vol. 76, 1994, pp. 1871.

30. Warren, B.E.: *X-ray Diffraction.*, Reading, MA: Addison-Wesley, 1969.

31. Klug, H.P. and L.E. Alexander: *X-ray Diffraction Procedures for Polycrystalline and Amorphous Materials.*, New York: John Wiley & Sons, 1954.

32. Berry, C.R.: Phys. Rev., Vol. 72, 1947, pp. 942.

33. Cullity, B.D.: *Elements of X-ray Diffraction.*, Reading, MA: Addison-Wesley, 1978.

34. Koren, G., R.J. Baseman, A. Gupta, M.I. Lutwyche, and R.B. Laibowitz: Appl. Phys. Lett., Vol. 56, 1990, pp. 2144.

35. Bhattacharya, D., R.K. Singh, and P.H. Holloway: J. Appl. Phys., Vol. 70, 1991, pp. 5433.

36. Bannister, M.K.: *Toughening of Brittle Materials by Ductile Inclusions,* Ph.D. in Cambridge, 1989.

37. Ashby, M., F.J. Blunt, and M.K. Bannister: Acta Metal., Vol. 37, 1989, pp. 1847.

38. Evans, A.G. and J.W. Hutchinson: Int. J. Solids and Struct., Vol. 20, 1984, pp. 455.

39. Suo, Z., C.F. Shih, and A.G. Varias: Acta Met. et Mater., Vol. 41, 1994, pp. 1551.

40. Duffey, T.P., T.G. McNeela, J. Mazumder, and A.L. Schawlow: Applied Physics Letters, Vol. 63, 1993, pp. 2339.

41. Duffey, T.P., T.G. McNeela, T. Yamamoto, J. Mazumder, and A.L. Schawlow: Physical Review B15, Vol. 51, 1995, pp. 14652-14663.

42. Duffey, T.P., T.G. McNeela, J. Mazumder, and A.L. Schawlow: in International Conference on Applicationsof Lasers and Electro-Optics (ICALEO'93). Orlando: Laser Institute of America, P. Denney, I. Miyamoto, and B.L. Mordike, 1993, pp. 127.

43. Kar, A. and J. Mazumder: Phys. Rev. E, Vol. 49, 1994, pp. 410.

44. Funk, D.S., J.W. Carlson, and J.G. Eden: Electronics Lett., Vol. 30, 1994, pp. 1859.

Appendix A. List of Publications (during the contract period for AFOSR 92-0142)

1. "A Laser Ablation Model to Produce Nanoscale Particles," in *Proceedings of the International Conference on Lasers and Electro-Optics (ICALEO'93),* vol. 77, P. Denney, I. Miyamoto, and B.L. Mordike (eds.), published by Laser Institute of America, p. 193, 1994 (with A. Kar).

2. "Mathematical Model for Laser Ablation to Generate Nanoscale and Submicrometer-Size Particles," *Physical Review E* **49**, p. 410, 1994 (with A. Kar).

3. "Nano-crystalline Materials by Laser Ablation," in *Laser Materials Processing IV,* J. Mazumder, K. Mukherjee, and B.L. Mordike (eds.), published by The Minerals, Metals and Materials Society, p. 255, 1994 (with A. Kar, T.P. Duffey, T. Yamamoto, T. McNeela, and A.L. Schawlow)

4. "Absorption Spectroscopic Measurements of Plume Density and Temperature in Production of Nano-crystalline $NbAl_3$ by Laser Ablation Deposition," *Physical Review B15* **51**, p. 14652, 1995 (with T.P. Duffey, T. Yamamoto, T.G. McNeela, and A.L. Schawlow).

5. "Synthesis of Nanocrystalline $NbA1_3$ by Laser Ablation Technique," submitted to *J.ournal of Nano-Crystalline Materials*, June 1995(with T. Yamamoto).

6 "Synthesis and Charecterization of Nano-Crystalline $NbAl_3$ by Laser Ablation Technique," in preparation for submission to *Metallurgical Transactions A.* (with T. Yamamoto).